

Chapter 1

Theoretical Background and Literature

This ability to confine light below the diffraction limit can be achieved by exploiting plasmons. By transferring energy from a diffraction-limited photonic field into resonantly polarised, collective oscillations of conduction electrons an enhanced electric field can be generated on the surface of a metallic nanostructure with nanoscale localisation. It is through the understanding and application of this phenomena that sub-wavelength optics is made possible. This chapter deals firstly with electromagnetic waves in media and the optical properties of metals. From this basis the existence of plasmons can be explained, including the different types of plasmons and how they interact. Finally, the plasmonics of metallic tips is discussed as these are of the structures primary dealt with in this project.

1.1 Plasmons

Plasmons are a direct solution of Maxwell's equations at the boundary between a dielectric and a metal. Despite plasmons existing on length scales from $\mathcal{O}(100 \text{ nm})$ to $\mathcal{O}(1 \text{ nm})$, the high free electron density of metals means that energy levels still retain their characteristic continuous conduction bands and [quantum/quantisation](#) effects can be ignored. Classical theory is able to accurately describe physical phenomena until the characteristic length scale drops below $\sim 0.5 \text{ nm}$. A phenomenological approach using Maxwell's equations [1] therefore forms the basis of the mathematical description of plasmons.

1.1.1 Electromagnetic Waves

Maxwell's equations universally describe the classical, dynamical behaviour of electromagnetic (EM) waves and form the foundations of electromagnetism. In their differential form they are

given by,

$$\nabla \cdot \mathbf{E} = \frac{\rho_{\text{tot}}}{\varepsilon \varepsilon_0}, \quad (1.1a)$$

$$\nabla \cdot \mathbf{B} = 0, \quad (1.1b)$$

$$\nabla \times \mathbf{E} = -\frac{\partial \mathbf{B}}{\partial t}, \quad (1.1c)$$

$$\nabla \times \mathbf{B} = \mu \mu_0 \left(\mathbf{J} + \varepsilon \varepsilon_0 \frac{\partial \mathbf{E}}{\partial t} \right), \quad (1.1d)$$

where \mathbf{E} is the electric field, \mathbf{B} is the magnetic flux density, ε_0 is the permittivity of free space, μ_0 is the permeability of free space, ρ_{tot} is the (volume) charge density, \mathbf{J} is the current density and t is time. The variables ε and μ are the relative permittivity and permeability, respectively, and describe the electromagnetic properties of the medium in which the wave exists. This set of partial differential equations describe the microscopic fields within an electromagnetic system. Two new quantities can be introduced to include material dependencies and describe the macroscopic fields. These are the *electric displacement field* \mathbf{D} and the *magnetic field* \mathbf{H} , defined as,

$$\mathbf{D} = \varepsilon_0 \mathbf{E} + \mathbf{P}, \quad (1.2a)$$

$$\mathbf{H} = \frac{1}{\mu_0} \mathbf{B} + \mathbf{M}, \quad (1.2b)$$

where \mathbf{P} is the polarisation (dipole moment per unit volume) and \mathbf{M} the magnetisation. The displacement field arises due to polarisation of a material in response to an applied field and is related to the internal charge density by $\nabla \cdot \mathbf{P} = \rho_{\text{int}}$. Conservation of charge means that $\nabla \cdot \mathbf{J} = \partial \rho / \partial t$, which requires that $\mathbf{J} = \partial \mathbf{P} / \partial t$ (a result also achievable by differentiating (1.2a)). The final equation of importance is the relationship between the electric field and the current density, given by,

$$\mathbf{J} = \sigma \mathbf{E}, \quad (1.3)$$

where σ is the conductivity. These few relations are sufficient to understand the behaviour of electromagnetic waves in media.

By utilising (1.2a), equations (1.1a) and (1.1d) can be redefined to include material dependencies as,

$$\nabla \cdot \mathbf{D} = \rho_{\text{ext}}, \quad (1.4a)$$

$$\nabla \times \mathbf{H} = \mathbf{J}_{\text{ext}} + \frac{\partial \mathbf{D}}{\partial t}. \quad (1.4b)$$

The charge and current densities now refer to only the external contributions, related to the

internal contributions via $\rho_{\text{tot}} = \rho_{\text{ext}} + \rho_{\text{int}}$ and $\mathbf{J}_{\text{tot}} = \mathbf{J}_{\text{ext}} + \mathbf{J}_{\text{int}}$. Propagation of EM waves within a medium is governed by a wave equation relating both the spatial and temporal changes of a wave. In general, a wave equation describing a wave $\psi(x)$ along an axis x in time t is of the form,

$$\frac{\partial^2 \psi}{\partial x^2} = \frac{1}{v^2} \frac{\partial^2 \psi}{\partial t^2}, \quad (1.5)$$

where v is the speed of the wave. Combining (1.1c) and (1.1d) leads to the general wave equation for EM waves in the time domain,¹

$$\nabla(\nabla \cdot \mathbf{E}) - \nabla^2 \mathbf{E} = -\varepsilon \varepsilon_0 \mu \mu_0 \frac{\partial^2 \mathbf{E}}{\partial t^2} - \mu \mu_0 \mathbf{J}, \quad (1.6)$$

$$\nabla(\nabla \cdot \mathbf{D}) - \nabla^2 \mathbf{D} = \frac{\partial^2 \mathbf{D}}{\partial t^2} - \mathbf{J}_{\text{ext}}, \quad (1.7)$$

describing the propagation of an electromagnetic wave in a given medium. In the absence of both charge and current (1.7) reduces to,

$$\nabla^2 \mathbf{E} = \varepsilon \varepsilon_0 \mu \mu_0 \frac{\partial^2 \mathbf{E}}{\partial t^2}, \quad (1.8)$$

describing a wave propagating in both space and time with a velocity c . Comparison to (1.5) shows that the speed of light in free space ($\varepsilon = \mu = 1$) is $c = 1/\sqrt{\varepsilon_0 \mu_0}$. Furthermore, the refractive index is defined as $\tilde{n} = \sqrt{\varepsilon \mu}$ such that $\varepsilon \varepsilon_0 \mu \mu_0 = (\tilde{n}/c)^2 = 1/v^2$. Waves are therefore slowed down by a factor \tilde{n} inside a medium.

In general ε is a complex quantity, $\varepsilon = \varepsilon_1 + i\varepsilon_2$, and depends on the frequency of the EM wave ω . Plasmons are a phenomena resulting from this frequency dependence in metallic materials. The relative permittivity is therefore denoted $\varepsilon(\omega)$ and is referred to as the dielectric function of a material from this point onwards. For this reason equations are simplified by removing any magnetic contributions by assuming $\mu = 1$. Since $\varepsilon(\omega)$ is a complex parameter $\tilde{n} = \sqrt{\varepsilon(\omega)} = \sqrt{\varepsilon_1 + i\varepsilon_2}$, the complex refractive index can be expressed as $\tilde{n} = n + i\kappa$, where n is the real part causing refraction and κ is the extinction coefficient determining absorption in the medium. The complex refractive index and the dielectric function are then related via $\varepsilon_1 = n^2 - \kappa^2$ and $\varepsilon_2 = 2n\kappa$.

If the material dielectric properties in ε are linear then \mathbf{D} can be expressed in Fourier space as,

$$\mathbf{D}(\mathbf{k}, \omega) = \varepsilon_0 \varepsilon(\mathbf{k}, \omega) \mathbf{E}(\mathbf{k}, \omega). \quad (1.9)$$

Combining (1.9) with the differential of (1.2a), (1.3) and a harmonic wave solution² yields the

¹Derived using $\nabla \times \nabla \times \mathbf{E} = \nabla(\nabla \cdot \mathbf{E}) - \nabla^2 \mathbf{E}$

² $\partial/\partial t \rightarrow -i\omega$ and $\mathbf{J} = \dot{\mathbf{D}} - \varepsilon_0 \dot{\mathbf{E}} = \varepsilon_0 \dot{\mathbf{E}}(\varepsilon - 1) = \sigma \mathbf{E}$

relationship between a material's conductivity and it's dielectric function,

$$\varepsilon(\mathbf{k}, \omega) = 1 + \frac{i\sigma(\mathbf{k}, \omega)}{\varepsilon_0 \omega}. \quad (1.10)$$

Depending on which is more convenient, either the dielectric function or the conductivity can be used to describe the optical response of a material. Conductivity is typically used to describe lower frequency phenomena while the dielectric function is used at higher frequencies.

The dispersive properties of a material are found by solving (1.7) with $\varepsilon = \varepsilon(\omega)$, describing the behaviour of a wave propagating through a non-magnetic, dielectric medium. For a monochromatic, harmonic wave with frequency ω and wave vector \mathbf{k} in space r of the form,

$$\mathbf{E} = \mathbf{E}_0 e^{i(\mathbf{k} \cdot \mathbf{r} - \omega t)}, \quad (1.11)$$

representing a propagating EM wave, (1.7) can be expressed in the frequency (Fourier) domain as,³

$$\mathbf{k}(\mathbf{k} \cdot \mathbf{E}) - k^2 \mathbf{E} = -\varepsilon(\mathbf{k}, \omega) \frac{\omega^2}{c^2} \mathbf{E}, \quad (1.12)$$

where $k = |\mathbf{k}|$ is the magnitude of the wavevector. The variable $k_0^2 = \omega^2/c^2$ is sometimes used in (1.12) when all quantities considered are wave vectors. From this equation the propagation behaviour of EM waves in media can be described.

Solutions to (1.12) depend on the orientation of the wavevector with the field. Transverse wave solutions ($\mathbf{k} \cdot \mathbf{E} = 0$) yield the dispersion relation for light,

$$k = \sqrt{\varepsilon(\mathbf{k}, \omega)} \frac{\omega}{c} = \tilde{n} k_0. \quad (1.13)$$

Inserting this into (1.11) gives a general solution for light propagating through a dielectric medium,

$$\mathbf{E}(\mathbf{r}) = \mathbf{E}_0(\mathbf{r}) \exp\left(-\kappa \frac{\omega}{c} \hat{\mathbf{k}} \cdot \mathbf{r}\right) \exp\left(i\omega\left(\frac{n}{c} \hat{\mathbf{k}} \cdot \mathbf{r} - t\right)\right). \quad (1.14)$$

The real component of the refractive index n slows the wave whereas the imaginary component corresponds to an exponential decay with characteristic length $1/\kappa$, representing loss within a medium. Since the real part of the conductivity is related to the imaginary part of the dielectric function the decay is attributed to energy transfer to move electrons at the surface of the material. Longitudinal wave solutions ($\mathbf{k} \cdot \mathbf{E} = k|\mathbf{E}|$) result in $\sqrt{\varepsilon(\mathbf{k}, \omega)}\omega/c = 0$, hence solutions only exists for $\varepsilon(\mathbf{k}, \omega) = 0$. Both these conditions are important when describing plasmons. Furthermore, when considering the behaviour of EM waves at an interface between two different media the orientation of the fields with respect to the interface becomes im-

³Derived using the identities $\nabla \times \nabla \times \mathbf{E} = \nabla(\nabla \cdot \mathbf{E}) - \nabla^2 \mathbf{E}$, $\nabla^2 \mathbf{E} = -k^2 \mathbf{E}$ and $\partial^2 \mathbf{E}/\partial t^2 = -\omega^2 \mathbf{E}$ where $\nabla \cdot \mathbf{E} = 0$

portant. Separate solutions exist depending on if a wave is considered transverse magnetic (TM) or transverse electric (TE) (either only \mathbf{E} or \mathbf{H} has a component in the direction of propagating, respectively).⁴

Using the framework outlined so far the optical properties of metals can be deduced along with the existence of plasmons. The discussion begins with the Drude model for the optical response of metals [2], which is used to first predict the behaviour of plasmons. From there the distinction can be made between plasmons within the volume of a metal and those confined to the surface, which are of most interest in plasmonics.

1.1.2 Bulk Plasmons and the Optical Properties of Metals

Before studying the concept of a surface plasmon it is important to understand the optical properties of metals in general. When light is incident on a metal, free electrons at the surface respond to the field and are displaced in the opposite direction (since $\mathbf{F} = -e\mathbf{E}$). The field of the induced charge distribution cancels the electric field inside the metal. An EM wave impinging on a metal is internally screened, and therefore externally reflected⁵, through the displacement of free electrons inside the metal surface. The reflected wave gives metals their shiny appearance. This behaviour originates from (1.10), where a high conductivity increases absorption and reduces the field penetration inside the metal. The exponential decay of the wave into the metal, shown in (1.14), is characterised by the skin depth $\delta_m = c/2\omega\kappa$, the point at which the field has decayed by 1/2e of its original value.⁶ The small values of δ_m exhibited by metals means that they fall within the *perfect conductor* approximation (zero internal field). Light transmission through a metal becomes heavily attenuated once its thickness becomes greater than δ_m .

A metal becomes more dielectric once the light oscillates fast enough that the inertia of the massive electrons means they cannot respond fast enough, preventing screening and thus transmitting the incident light. Such effects begin to be seen around the visible spectrum of light in noble metals. Fields increasingly penetrate the metal until photon energies in the UV spectrum are reached, at which point most metals become transparent. This is known as the *ultraviolet transparency*. These effects can be seen by simply considering the response of a free electron gas to an applied field.

Unlike many other materials whose optical properties are determined by the response of bound electrons (described by the Lorentz oscillator model), the properties of metals are dominated by the response of free electrons delocalised from the positive nuclei background. The Drude model [2] is a simple description of the optical properties of metals and describes

⁴TE and TM are also known as *s*- and *p*-polarisations, respectively.

⁵Light absorbed by electrons will be re-emitted, or from a different point of view, the prevention of light from entering the metal means the incident field must be reflected.

⁶The skin depth is defined using 1/2e rather than 1/e to consider power instead of field.

the motion of a free electron gas in response to an applied field. The equation of motion for a single electron in a time-varying applied field is given by,

$$m\ddot{\mathbf{x}}(t) + m\gamma\dot{\mathbf{x}}(t) = -e\mathbf{E}(t), \quad (1.15)$$

where m is its effective optical mass and $\gamma = 1/\tau$ is the electron collision frequency, the inverse of the relaxation time τ . Use of an effective optical mass as opposed to the actual electron mass incorporates band structure effects into the model. The electron collision frequency amounts to an effective coefficient of damping as in a mechanical oscillator. Inserting a harmonic driving field and assuming a similar oscillatory behaviour in the free electron displacement ($\mathbf{x} = \mathbf{x}_0 e^{-i\omega t}$) leads to a solution,

$$\mathbf{x}(t) = \frac{e}{m(\omega^2 + i\gamma\omega)} \mathbf{E}(t). \quad (1.16)$$

There is a resulting polarisation $\mathbf{P} = -n\epsilon\mathbf{x}$ induced in the free electron gas, where n is the number density of electrons. The resulting displacement field, **acquired** by substituting (1.16) into (1.9)⁷, defines the dielectric function of a metal,

$$\epsilon(\omega) = 1 - \frac{\omega_p^2}{\omega^2 + i\gamma\omega}, \quad (1.17)$$

where ω_p is the plasma frequency of the metal, given by,

$$\omega_p^2 = \frac{ne^2}{\epsilon_0 m}. \quad (1.18)$$

The optical properties of a metal can be discerned from the real and imaginary components of $\epsilon(\omega)$, given by,

$$\text{Re}[\epsilon(\omega)] = \epsilon_1(\omega) = 1 - \frac{\omega_p^2\tau^2}{1 + \omega^2\tau^2}, \quad (1.19a)$$

$$\text{Im}[\epsilon(\omega)] = \epsilon_2(\omega) = \frac{\omega_p^2\tau}{\omega(1 + \omega^2\tau^2)}. \quad (1.19b)$$

Metallic physical characteristics correspond to $\text{Re}[\epsilon(\omega)] < 0$, **i.e.** **D negative compared to E**, where electrons move to oppose an incident field. The plasma frequency defines the point at which the metal transitions into a dielectric. For $\omega < \omega_p$, $\text{Re}[\epsilon(\omega < \omega_p)] < 0$ and a free electron gas remains metallic in character. Once $\omega > \omega_p$ the free electron gas, **limited by inertia**, cannot respond fast enough to follow the field and becomes dielectric in character.

⁷Derived from $\mathbf{D} = \epsilon_0\mathbf{E} + \mathbf{P} = \epsilon_0\mathbf{E} - [ne^2/m(\omega^2 + i\gamma\omega)]\mathbf{E} = \epsilon_0\epsilon(\omega)\mathbf{E}$

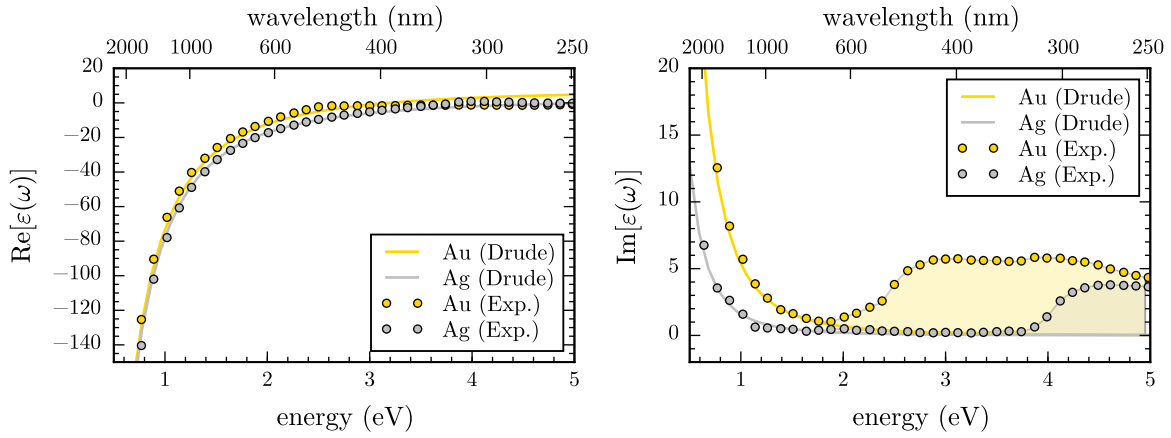


Figure 1.1: Plot of the dielectric function, given by the Drude model, for Au and Ag compared with empirical data. $\varepsilon(\omega)$ is calculated using (1.21). The plasma frequency is calculated using (1.18). The parameters of the curves are $n = 5.90 \times 10^{28} \text{ m}^{-3}$, $m = 9.11 \times 10^{-31} \text{ kg}$, $\gamma = 1/\tau = 1/1 \times 10^{-14} \text{ s}$ and $\varepsilon_\infty = 8$ for Au and $n = 5.86 \times 10^{28} \text{ m}^{-3}$, $m = 9.11 \times 10^{-31} \text{ kg}$, $\gamma = 1/\tau = 1/3 \times 10^{-15} \text{ s}$ and $\varepsilon_\infty = 3$ for Ag. Empirical data (Johnson and Christy, 1972 [3]) is shown for comparison to illustrate the importance of interband transitions. Deviations from the Drude model due to interband transitions are shaded.

For an ideal free electron gas with negligible damping the expression,

$$\varepsilon(\omega) = 1 - \frac{\omega_p^2}{\omega^2}, \quad (1.20)$$

is often used. This is the often the case for large (**optical**) frequencies close to ω_p where the imaginary component of $\varepsilon(\omega)$, dominated by $\omega\tau \gg 1$, becomes negligible. In actually, however, interband transitions in real metals increase $\text{Im}[\varepsilon(\omega)]$. The expression for the dielectric function can be modified to account for interband absorption caused by bound electrons by the inclusion of a constant ε_∞ . The dielectric function then has the form,

$$\varepsilon(\omega) = \varepsilon_\infty - \frac{\omega_p^2}{\omega^2 + i\gamma\omega}. \quad (1.21)$$

Plotting (1.21), along with empirical data, illustrates both why noble metals exhibit high quality visible spectrum (400–700 nm, 1.5–3 eV) plasmonics as well as the failings of the Drude model. Noble metals have $\text{Re}[\varepsilon(\omega)] < 0$ and small $\text{Im}[\varepsilon(\omega)]$ in the visible region, hence behave very similar to an ideal free electron gas. The Drude model fails at higher energies as interband transitions are not included in the basic model. These transitions increase the absorption ($\propto \text{Im}[\varepsilon(\omega)]$) and are significant for $\lambda < 500 \text{ nm}$ in Au and $\lambda < 300 \text{ nm}$ in Ag. A measure of the quality of a plasmonic material can de determined from its quality factor $Q = |\text{Re}[\varepsilon]/\text{Im}[\varepsilon]|$. The high Q of noble metals in the visible regions means they can easily respond to an incident field and screen it, behaving plasmonically. Interband transitions lead

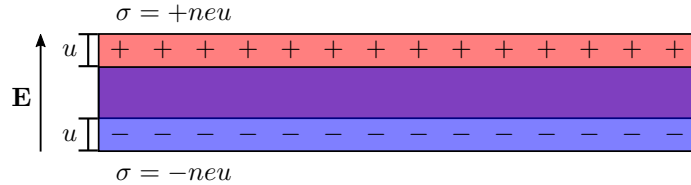


Figure 1.2: Charge displacement of a free electron gas under an applied field. The optical electric field displaces the electrons leaving behind the positive cores. The slab becomes polarised with opposing surface charge densities σ . The charge oscillations resonate when the field frequency is ω_p .

to a reduction in Q at higher energies therefore preventing good plasmonics.

The significance of the plasma frequency ω_p in $\varepsilon(\omega)$ is that it not only describes a metal-to-dielectric transition but also dictates the frequency of the collective longitudinal mode of oscillation. By substituting (1.20) into the dispersion relations for transverse and longitudinal waves it is clear that transverse waves are only supported if $\omega > \omega_p$ with dispersion $\omega^2 = \omega_p^2 + k^2c^2$. However, a collective longitudinal oscillation is allowed at $\omega = \omega_p$ since $\varepsilon(\omega) = 0$ in the absence of damping. In this case the free electron gas is displaced from the ionic core background a distance u due to the applied field to form surface charge densities $\sigma = \pm neu$. The resulting depolarisation field⁸ is $\mathbf{E} = neu/\varepsilon_0$ and the motion of the free electrons are defined by,

$$nm\ddot{u} = -ne\mathbf{E} = -\frac{n^2e^2u}{\varepsilon_0}. \quad (1.22)$$

Simplifying this relation leads to,

$$\ddot{u} + \omega_p^2 u = 0, \quad (1.23)$$

hence ω_p is considered the natural frequency of the system and the electrons resonate when driving at $\omega = \omega_p$. This is known as the bulk or *volume plasmon*. Since this is a longitudinal oscillation, however, light cannot couple with a volume plasmon. Experimentally these are measured using electron energy loss spectroscopy (EELS), whereby colliding electrons impart energy and excite a volume plasmon [4]. Observation of optical plasmonic phenomena therefore means that light-matter plasmonics is the result of a different kind of plasmon.

1.1.3 Surface Plasmons, Surface Plasmon Polaritons and Localised Surface Plasmon Polaritons

Surface plasmons (SPs), unlike bulk plasmons, are tightly confined to the surface of the metal. As stated previously, light at an interface is not necessarily restricted by the diffraction limit. The maximum magnitude of the wavevector is set by $k_0 = 2\pi/\lambda$ with individual components

⁸Gauss' law $\int \mathbf{E} \cdot d\mathbf{A} = Q/\varepsilon_0 = \sigma A/\varepsilon_0$, hence $\mathbf{E} = \sigma/\varepsilon_0$. Alternatively $D = 0 = \varepsilon_0 \mathbf{E} + \mathbf{P}$ therefore $\mathbf{E} = -\mathbf{P}/\varepsilon_0 = -ne\mathbf{u}/\varepsilon_0$.

restricted by $k = \sqrt{k_x^2 + k_y^2 + k_z^2}$. Consider (1.13) in the form,

$$k_x^2 = \tilde{n}^2 k_0^2 - k_y^2 - k_z^2. \quad (1.24)$$

If a wave propagates freely in all three dimensions then it remains diffraction limited and the propagation constant $k_x < \tilde{n}k_0$. However if one or more of its wavevector components become imaginary ($k_{y,z}^2 < 0$) then it becomes possible that $k_x > \tilde{n}k_0$. This behaviour can occur at an interface, where surface waves take on evanescent character in the z -direction whilst propagating in the xy plane.⁹ By coupling light into surface waves the diffraction limit can be beaten. Waves of frequency ω can acquire wavelengths many times smaller than their excitation wavelength. The SP is one such case of this phenomenon and occurs at metal-dielectric interfaces. Unlike in the bulk of a metal, electrons displaced by an applied field at the surface of a metal do feel a restoring force with the positive nuclei background. Transverse fields impinging on the metal surface at an angle are then able to manipulate the electron motion. SPs can therefore be manipulated by light as well as by the longitudinal waves needed to excite bulk plasmons. They also have the ability to form polariton quasiparticles under strong coupling with photons, hence they are optically excitable under the right conditions.¹⁰ This optical excitation is known as the surface plasmon polariton (SPP) and, as a result of it being optically accessible, is one of the most commonly studied plasmonic phenomena.

Surface Plasmon Polaritons

A SPP is a propagating TM wave confined to the surface of a metal and the bound state between a photon and a SP. While confined in two dimensions to the planar boundary between a metal and a dielectric, the SPP can either propagate or become stationary as a result of interference **with itself or other plasmons**. The latter stationary form of the SPP is similar to the localised surface plasmons described later.

The SPP itself is described through its dispersion. As a TM wave propagating in the x -direction along a metal/dielectric interface its field profile is given by $\mathbf{E}(\mathbf{x}) = \mathbf{E}(z)e^{i\beta x}$ where $\beta = k_x$ is the propagation constant. The magnetic field in this configuration is then $\mathbf{H}(\mathbf{x}) = \mathbf{H}(y)e^{i\beta x}$. The behaviour of such a wave in (1.12) is described by,

$$\frac{\partial^2 \mathbf{E}(z)}{\partial z^2} + (k_0^2 \varepsilon - \beta^2) \mathbf{E} = 0, \quad (1.25a)$$

$$\frac{\partial^2 \mathbf{H}(y)}{\partial y^2} + (k_0^2 \varepsilon - \beta^2) \mathbf{H} = 0, \quad (1.25b)$$

⁹Evanescence meaning imaginary k_z therefore exponentially decaying amplitude in the z -direction.

¹⁰Polaritons are the name given to quanta or quasiparticles of light-matter interactions. Strong coupling describes the point at which a quasiparticle is no longer distinguishable between its two constituent components.

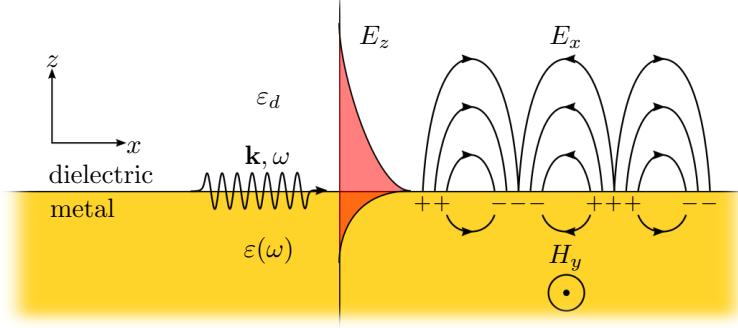


Figure 1.3: Diagram of a surface plasmon polariton (SPP). TM surface electron density waves (surface plasmons) couple with an evanescent wave originating from an EM wave to form a SPP. The SPP remains confined to the interface but can propagate across the surface.

which can be solved under the appropriate boundary conditions to yield the properties of a SPP. Assuming a TM wave ($\partial E_y / \partial z = 0, \partial H_z / \partial z = 0$), propagating only in the x -direction with symmetry in y -direction, results in outcomes from (1.1c) and (1.1d) of,

$$E_x = -i \frac{1}{\omega \varepsilon_0 \varepsilon} \frac{\partial H_y}{\partial z}, \quad (1.26a)$$

$$E_z = -\frac{\beta}{\omega \varepsilon_0 \varepsilon} H_y. \quad (1.26b)$$

In this instance the TM wave equation, and requirement for evanescent decay in the z -direction, mean that $H_y = A_d e^{i\beta x} e^{k_d z}$ for $z > 0$ (in the dielectric) and $H_y = A_m e^{i\beta x} e^{k_m z}$ for $z < 0$ (in the metal). The components of the electric field can therefore be expressed as,

$$E_x(z) = i A_d \frac{1}{\omega \varepsilon_0 \varepsilon_d} k_d e^{i\beta x} e^{-k_d z}, \quad (1.27a)$$

$$E_z(z) = -A_d \frac{\beta}{\omega \varepsilon_0 \varepsilon_d} e^{i\beta x} e^{-k_d z}, \quad (1.27b)$$

inside the dielectric and,

$$E_x(z) = -i A_m \frac{1}{\omega \varepsilon_0 \varepsilon_m} k_m e^{i\beta x} e^{k_m z}, \quad (1.28a)$$

$$E_z(z) = -A_m \frac{\beta}{\omega \varepsilon_0 \varepsilon_m} e^{i\beta x} e^{k_m z}, \quad (1.28b)$$

inside the metal, where $\varepsilon_1 = \varepsilon_d$ and $\varepsilon_m = \varepsilon(\omega)$ in the previously used notation. Continuity across the boundary ($z = 0$) dictates that $A_d = A_m$ and yields the relation,

$$\frac{k_2}{k_1} = -\frac{\varepsilon_m}{\varepsilon_d}, \quad (1.29)$$

hence the ratio between wavevectors inside and outside of the metal depends on the relative

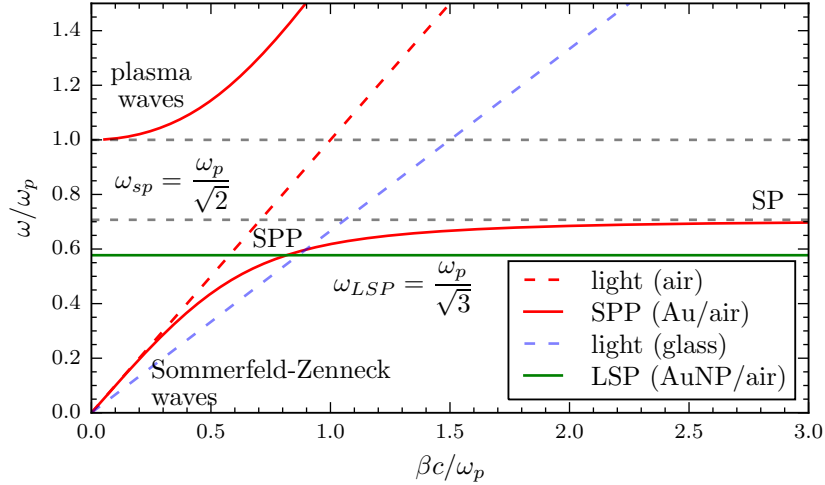


Figure 1.4: Plasmon dispersion relations for the SPP and LSP. The dashed lines indicate the dispersion of light in both glass and air (vacuum) along with the surface plasmon frequency. SPPs can be described as photon-like or plasmon-like depending on their point of excitation. SPPs excited with large k and $\omega \approx \omega_{SPP}$ are considered plasmon-like while SPPs with low k are considered more photon-like.

change in dielectric constant across the boundary. It is this continuity relation that allows for the existence of SPPs in the TM configuration, unlike for TE waves for which this result is not possible. To determine the SPP propagation constant β a further relation is needed to fix the wave vectors in a given medium with respect to the dielectric constant. Using the expression for H_y in the wave equation (1.12) yields a set of relations,

$$k_m^2 = \beta^2 - k_0^2 \varepsilon_m, \quad (1.30a)$$

$$k_d^2 = \beta^2 - k_0^2 \varepsilon_d, \quad (1.30b)$$

which, when combined with (1.29), fully describe the fields around the interface. The propagation constant is then given by,

$$\beta = \frac{\omega}{c} \sqrt{\frac{\varepsilon_d \varepsilon(\omega)}{\varepsilon_d + \varepsilon(\omega)}}. \quad (1.31)$$

This is the dispersion relation for a SPP and describes many of their important properties.

The SPP dispersion described by (1.31) is shown in Figure 1.4 along with the dispersion of light for both air and glass media. From the dispersion curve it is clear that SPPs cannot couple with light within the same medium as their dispersion curves do not cross. However, light from within a higher refractive index medium such as glass can generate evanescent waves and excite SPPs on a nearby metal/air interface. This method of coupling photons with surface plasmons, depending on the specific prism arrangement, is known as the Kretschmann

(prism-metal-dielectric) or Otto (prism-dielectric-metal) configuration [5, 6]. Since a diffraction grating may also impart momentum onto a photon ($k_x \rightarrow k_x + n\pi$) a metallic grating can launch SPPs along a planar metal-dielectric interface. This phenomenon was first observed in 1902 by Wood, dubbed as Wood's anomaly [7], and only explained via surface waves many years later [8].

Closer inspection of the curve highlights one of the major features of a plasmon. While SPPs retain the frequency of the excitation field, their wavelength is considerably smaller than the diffraction-limited wavelength of light. Depending on where on the curve the SPP lies it can be considered to be either more photon-like or more plasmon-like. For small $\beta \approx k_0$ the SPP is similar to light grazing the interface whereas SPPs with large k become more plasmon-like and their frequency saturates at the surface plasmon frequency,

$$\omega_{sp} = \frac{\omega_p}{\sqrt{1 + \varepsilon_d}}. \quad (1.32)$$

At this point the SPP can be considered electrostatic and becomes a SP. To some extent, SPs confined to a finite, continuous, non-planar surface, defining a nanoparticle (NP), can be considered to be the basis for a localised surface plasmon (LSP) **or localised surface plasmon polariton (LSPP)**.

Localised Surface Plasmons

LSPs are collective oscillations of conduction electrons confined within a fixed sub-wavelength spatial extent, usually on the surface of a metallic nanoparticle (MNP). Free electrons are displaced from the nuclei in response to an applied field and form a surface charge distribution, polarising the particle. Coulomb interaction between the poles of the surface charge distribution results in a restoring force within the particle. This gives rise to a natural frequency of oscillation, leading to a surface plasmon resonance (SPR) when driven harmonically at the correct frequency. The particle geometry sets which multipolar surface charge distributions are supported while its material properties and the dielectric properties of the surrounding medium set the restoring force. Each different multipolar charge distribution is therefore considered to be a unique LSP mode, identifiable by its SPR [9]. This bears some similarity with the slab of free electron gas supporting longitudinal volume plasmons, shown in Figure 1.2, except that the sub-wavelength geometry modifies the restoring force and allows transverse modes of oscillation. The plasma frequency in LSPs is then rescaled by a factor depending on the geometry of each LSP mode.

The simplest form of a LSP is the dipole resonance of a spherical MNP. Assuming the sphere radius, $a \ll \lambda$, the wavelength of light, the particle is considered to be in the quasistatic regime and electrostatics, rather than electrodynamics, is applicable to solve the problem. The

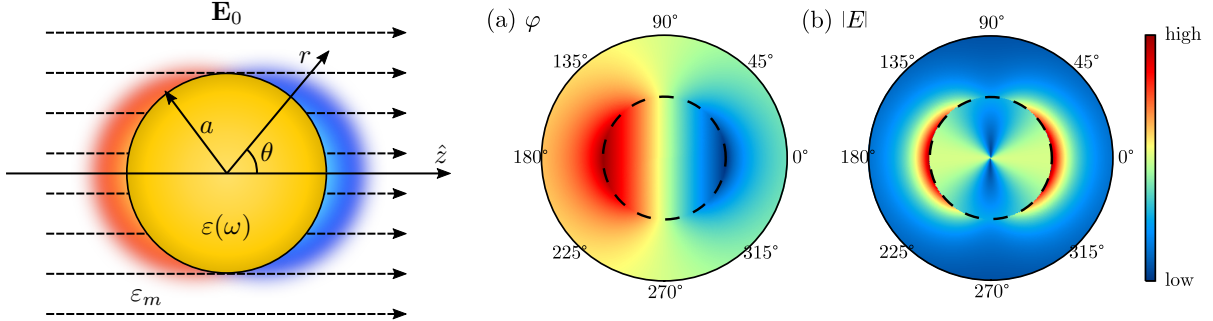


Figure 1.5: A spherical metallic particle in an applied electric field. The sphere is assumed to be in the quasistatic regime ($a \ll \lambda$). The aura around the particle indicates the phase of the free electron oscillations in the plasmon. Calculations of (a) the potential and (b) the magnitude of the electric field for a spherical nanoparticle on resonance ($\varepsilon(\omega) = -2\varepsilon_d$).

electrostatic potential, φ , of the system is described by the Laplace equation, $\nabla^2\varphi = 0$, with a general solution in a spherical geometry of the form,

$$\varphi_{l,m_l}(r, \theta, \phi) = \sum_{l=0}^{l=\infty} \sum_{m_l=-l}^l [A_l r^l + B_l r^{-(l+1)}] P_l^m(\cos \theta) e^{im_l \phi}, \quad (1.33)$$

where l is the degree of spherical harmonic and m_l its projection, A_l and B_l are constants and $P_l^m(\cos \theta)$ are associated Legendre polynomials. For a sphere of radius a and dielectric function $\varepsilon(\omega)$ in a dielectric medium described by ε_d the solution is fixed by the boundary conditions $\varphi_{\text{out}} \rightarrow -E_0 z$ as $r \rightarrow \infty$ and $\nabla \varphi_{\text{in}}(r)|_{r=a} = \nabla \varphi_{\text{out}}(r)|_{r=a}$. This reduces to a solution [10],

$$\varphi = \begin{cases} -\frac{3\varepsilon_d}{\varepsilon(\omega) + 2\varepsilon_d} \mathbf{E}_0 \cdot \mathbf{r} & r \leq a \text{ (inside)}, \\ \left(-1 + \frac{\varepsilon(\omega) - \varepsilon_d}{\varepsilon(\omega) + 2\varepsilon_d} \frac{a^3}{r^3}\right) \mathbf{E}_0 \cdot \mathbf{r} & r > a \text{ (outside)}. \end{cases} \quad (1.34)$$

For a metal sphere the potential describes an induced dipolar surface charge distribution, as plotted in Figure 1.5a. The description is simplified by defining the dipole moment as,

$$\mathbf{p} = \varepsilon_0 \varepsilon_d \alpha \mathbf{E}_0 = 4\pi \varepsilon_0 \varepsilon_d a^3 \frac{\varepsilon(\omega) - \varepsilon_d}{\varepsilon(\omega) + 2\varepsilon_d} \mathbf{E}_0, \quad (1.35)$$

where the polarisability, α , incorporates the frequency dependent behaviour and is defined as,

$$\alpha(\omega) = 4\pi a^2 \frac{\varepsilon(\omega) - \varepsilon_d}{\varepsilon(\omega) + 2\varepsilon_d}. \quad (1.36)$$

The outside potential is then expressed as,

$$\varphi_{\text{out}} = -\mathbf{E}_0 \cdot \mathbf{r} + \frac{\mathbf{p} \cdot \mathbf{r}}{4\pi \varepsilon_0 \varepsilon_d r^3}. \quad (1.37)$$

The potential of the system is simply the potential of a dipole superimposed onto the incident field. The electric field inside and outside of the sphere is calculated using $\mathbf{E} = -\nabla\varphi$, resulting in,

$$\mathbf{E} = \begin{cases} \frac{3\varepsilon_d}{\varepsilon(\omega) + 2\varepsilon_d} \mathbf{E}_0 & r \leq a \text{ (inside)}, \\ \mathbf{E}_0 + \frac{3\mathbf{n}(\mathbf{n} \cdot \mathbf{p}) - \mathbf{p}}{4\pi\varepsilon_0\varepsilon_d} \frac{1}{r^3} & r > a \text{ (outside)}, \end{cases} \quad (1.38)$$

where $\mathbf{n} = \mathbf{r}/r$ is the unit vector. As with the potential, the electric field is the superposition of the incident field with the field emitted from a point dipole, shown in Figure 1.5b.

It is assumed from its sub-wavelength size that electrons in the sphere respond instantaneously to the incident field and phase retardation is ignored (quasistatic approximation). Under this assumption the electrostatic result is simply multiplied with a harmonic time dependence to describe electrodynamic behaviour. Therefore, when illuminated by a plane wave $\mathbf{E}_0 e^{i\omega t}$ the induced dipole moment oscillates like $\mathbf{p} e^{i\omega t}$. In this sense the coherent oscillation of free electrons in the sphere is considered to be an oscillating point dipole source given by $\mathbf{p} e^{i\omega t} = \varepsilon_0 \varepsilon_d \alpha \mathbf{E}_0 e^{i\omega t}$. The physical behaviour of the electrons in the sphere, described using the dielectric function $\varepsilon(\omega)$, is then simply incorporated into $\alpha(\omega)$, at which point its frequency dependence becomes important.

For a good metal $\text{Re}[\varepsilon(\omega)] < 0$ and the denominator in (1.36) undergoes resonance whereby $\alpha \rightarrow -\infty$ when $\varepsilon(\omega) + 2\varepsilon_d \rightarrow 0$. Resonance therefore occurs at the Fröhlich condition when,

$$\text{Re}[\varepsilon(\omega)] = -2\varepsilon_d. \quad (1.39)$$

Resonant excitation of the induced oscillating dipole moment corresponds to excitation of a collective oscillation of conduction electrons on the surface of the sphere - the dipolar LSP. Its strength in realistic metals is restricted by damping of the electron motion leading to a Lorentzian-shaped resonance band - the dipolar SPR. As seen in (1.38), the field from the induced dipole moment of the plasmon is superimposed onto the incident field leading to a resonant near-field enhancement, both inside and outside the surface of the sphere. This is one of the fundamental properties of the plasmon, and one that is most exploited in sensing and sensor developments.

Under the Drude model, with $\varepsilon(\omega)$ given by (1.21), the Fröhlich condition is satisfied when,

$$\omega_{lsp} = \frac{\omega_p}{\sqrt{1 + 2\varepsilon_d}}, \quad (1.40)$$

which evaluates to $\omega = \omega_p/\sqrt{3}$ for a MNP in vacuum. As can be seen in Figure 1.4, the flat dispersion of a LSP mode means it crosses the light line at a single point. Light of the correct frequency therefore readily couples with LSPs without the need for SPP momentum matching mechanisms. In general, the optical spectrum of a MNP can contain a number of multipolar

plasmon modes **other than the dipole mode** for which the resonant frequencies are given by,

$$\omega_l = \omega_p \sqrt{\frac{l}{\varepsilon_d(l+1)+1}}, \quad (1.41)$$

where the degree of spherical harmonics l denote the charge distribution and denoted mode order ($l = 1$ for dipole, $l = 2$ for quadrupole, etc.). However, these modes only exist outside of the quasistatic regime in larger MNPs or more complex geometries. For plasmonically-active nobles metals, such as Au and Ag, the fundamental $l = 1$ mode occurs in the visible spectrum ($\lambda = 520$ nm for Au and $\lambda = 360$ nm for Ag), leading to them often being the plasmonic metal of choice. Additionally, since the polarisability changes with NP geometry, changes from a spherical shape lead to tuning of the SPRs across the visible spectrum. This geometrical dependence is well known and has been measured experimentally on a number of occasions [11, 12].

As with any oscillating charge distribution, energy is both absorbed and emitted from the plasmon. The oscillating charge has the ability to scatter the incident planar field into spherical waves. The excitation of a resonant dipolar oscillation means that the scattering is also resonantly enhanced. The balance between the absorbance and the scattering from a MNP is dictated by its size. The absorbance and scattering cross sections are given by [13],

$$\sigma_{\text{scat}} = \frac{k^4}{6\pi} |\alpha|^2 = \frac{8\pi}{3} k^4 a^6 \left| \frac{\varepsilon(\omega) - \varepsilon_d}{\varepsilon(\omega) + 2\varepsilon_d} \right|^2, \quad (1.42a)$$

$$\sigma_{\text{abs}} = k \text{Im}[\alpha] = 4\pi k a^3 \text{Im} \left[\frac{\varepsilon(\omega) - \varepsilon_d}{\varepsilon(\omega) + 2\varepsilon_d} \right]. \quad (1.42b)$$

The extinction cross section, commonly used in spectroscopy, can be calculated using $\sigma_{\text{ext}} = \sigma_{\text{scat}} + \sigma_{\text{abs}}$. Since they depend on α the size of the cross section, i.e. the spatial extent over which light can interact with the MNP, is increased on resonance. This is why MNPs appear strongly coloured and much larger in optical microscopy than they actually are. The absorbance and scattering cross sections scale as a^3 and a^6 , respectively, hence larger particles scatter more than they absorb whereas absorption dominates in smaller particles.

From the cross-sections the relationship between the LSP near-field and the far-field is made clearer. On resonance with the dipolar LSP, both cross sections are enhanced by the polarisability resonance from $\mathcal{O}(a \sim 50 \text{ nm})$ to $\mathcal{O}(500 \text{ nm})$. The increased size of the cross-section is comparable to the wavelength of light meaning LSPs efficiently couple with photons in the far-field.¹¹ The LSP mediates energy transfer between the near-field and the far-field and acts to match the electromagnetic modes of nanoscale absorbers/emitters, such as

¹¹Consider that σ_{scat} for a AuNP is enhanced $100\times$ on resonance, meaning it's area cross-section is $\sqrt{100/\pi} = 6\times$ wider than it's radius, hence why a 50 nm AuNP looks like a 300 nm green sphere when imaged.

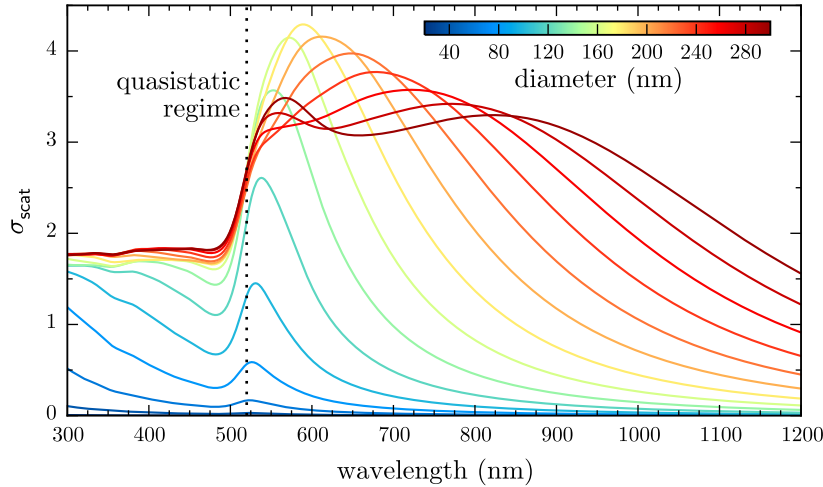


Figure 1.6: Mie scattering efficiencies/cross-sections for AuNPs of increasing diameter. The 520 nm resonance position of the dipolar LSP mode of a AuNP in the quasistatic approximation is indicated by the dotted line. The resonance stays at 520 nm until $d > 80$ nm then redshifts. The emergence of higher order modes following a similar behaviour is seen once $d > 100$ nm.

phonons (Raman) and radiative energy levels (quantum emitters, fluorescence), with those of a diffraction-limited photonic mode via an oscillating charge density [14]. A plasmonic NP is often therefore described as an *optical antenna* in a similar manner to a device that converts between radio waves and an electrical current is named a radio antenna. LSP modes which readily couple with the far-field are then sometimes referred to as *antenna modes* and become important when designing resonant structures for specific sensing applications.

Whilst the quasistatic approach is useful to first demonstrate the enhancing capabilities of a MNP, the description breaks down once the size of the particle becomes more comparable to the excitation wavelength. Retardation effects between the field and the electrons mean that phase differences between the charge oscillations and the incident field become important. At this point Mie theory (electrodynamics) is required to describe the spectral response of spherical MNPs [15]. Mie theory provides a more general description of the optical response of spherical MNPs. Using this approach the spectra of a MNP can be decomposed into superimposed multipoles, alluding to the existence of higher order LSP modes in larger MNPs. The spectral response of spherical AuNPs of varying sizes is shown in Figure 1.6, demonstrating the redshift and broadening of lower order modes with increasing particle size and the excitation of higher order modes.

Geometrical Influences on Localised Surface Plasmon Resonances

As previously stated, the LSP is a geometrical resonance and exists primarily due to the interplay between the driving field inducing oscillations in the mobile electrons and the resulting restoring force acting between the positive ionic core background and the accumulation of

conduction electrons at the surface. While the surface charge oscillation directly correlates to the driving field the restoring force, incorporated into the polarisability, is geometry dependent. The SPRs of a single particle are therefore very geometry dependent [11, 12, 16]. The larger the separation between opposing surface charge poles in the antenna, the weaker the restoring force. As seen with Mie theory, a larger particle with a smaller restoring force has a lower energy resonance. The same can be said if the particle geometry is elongated (a nanoellipsoid or nanorod). Within the quasistatic regime, the polarisability of an ellipsoidal MNP is adjusted by inserting a geometrical correction, leading to the redefinition,

$$\alpha_i(\omega) = 4\pi a_1 a_2 a_3 \frac{\varepsilon(\omega) - \varepsilon_d}{3\varepsilon_d + 3L_i(\varepsilon(\omega) - \varepsilon_d)}, \quad (1.43)$$

where i is the index of each anisotropic axis with a geometrical factor,

$$L_i = \frac{a_1 a_2 a_3}{2} \int_0^\infty \frac{dq}{(a_i^2 + q)\sqrt{(q + a_1^2)(q + a_2^2)(q + a_3^2)}}. \quad (1.44)$$

The resonance condition along each axis is then changed to,

$$\text{Re}[\varepsilon(\omega)] = -\frac{1 - L_i}{L_i} \varepsilon_d. \quad (1.45)$$

By decreasing the geometrical factor the resonance condition decreases from $-2\varepsilon_d$, corresponding to a decreased resonant frequency and a redshifted SPR. The longer the particle is, the larger the redshift until the particle is large enough to no longer be considered plasmonic. Continual separation of the poles inevitably weakens the restoring force to the point that each lowest-order antenna SPR no longer exists.

By utilising the particle material, geometry and polarisation anisotropy to tune the plasmon resonance, the resonant wavelength band can be shifted across the entire UV–NIR spectrum to tailor individual applications. The limitation to this technique is the relatively small field enhancement that a single particle can provide. An alternative approach to exploiting LSPs is therefore to couple the fields of many plasmons together. Through coupling the confined fields in the gaps between MNPs can be enhanced by many more orders of magnitudes.

1.2 Plasmon Coupling

Both the resonant field enhancement and the confinement of a surface plasmon can be improved by bringing a second plasmon into close proximity. Similar to coupled harmonic oscillators and dipoles, plasmons couple together via Coulomb forces once brought together, forming normal modes of oscillation across interacting charge distributions. In many cases the charge

distribution of the resulting normal mode is strongly confined to the dielectric space between metallic surfaces where charges strongly interact. Normal modes are therefore more generally known as *gap plasmons*. It is the existence of gap plasmons that has both enabled single molecule spectroscopy and resulted in the large degree of spectral tuning observed in composite plasmonic systems.

Coupled plasmons are a feature of many metallic nano-systems with closely spaced metal-dielectric interfaces, including metal-insulator-metal (MIM) and insulator-metal-insulator (IMI) waveguides and systems containing multiple MNPs. For the purposes of this work, discussion is restricted to the ideal case of coupled LSPs between two closely spaced MNPs, though the description of coupling is valid for many other cases involving SPs.

1.2.1 Localised Surface Plasmon Hybridisation in Nano-Gap Cavities

In the simplest case, only multipolar plasmons, excited in two spherical MNPs being driven by external EM fields, are considered. This is the prototypical plasmonic dimer system used to understand plasmon coupling. Similar systems, including chains of MNPs [17] and MNPs on mirrors [18, 19], have been used to study plasmon coupling. In each of these systems, the physics can be reduced to the interaction between neighbouring charge distributions. This is why the simple dimer system is important to fully understand.

The behaviour of a plasmonic dimer stems from the Coulomb interaction between free electrons in adjacent metallic nanostructures. As MNPs move closer together the force between charges grows, increasingly polarising the local gap region to which the charge becomes confined. The introduction of separation-dependent forces to the plasmon oscillator shifts the resonance frequency of the individual plasmon mode from ω_0 by $\Delta\omega$ depending on the strength of coupling. Since coupling is between multipolar fields, the relative orientation between excited LSPs and the external driving field is important to determine the sign and strength of coupling. Coupling is strongest when adjacent plasmon poles are oppositely charged. This is generally the case for LSPs in a MNP dimer being driven in phase with the incident field.

The primary effect of gap plasmon excitation is the localisation of the electric field to the dielectric gap medium. As stated previously, a plasmon intrinsically enhances the near-field around a MNP, caused by optically-driven charge accumulation at the metal-dielectric interface. For the case of two interacting plasmonic particles, the Coulomb forces between plasmons pulls charge more towards the gap region. As a result, a greater amount of charge accumulates on the metal surfaces around the gap and the field in the gap cavity becomes more localised and further enhanced.¹² For a strongly confined gap mode there is very little field

¹²This is much like with charged plates in a capacitor and how the field increases with dielectric gap material, spacing and charge accumulation.

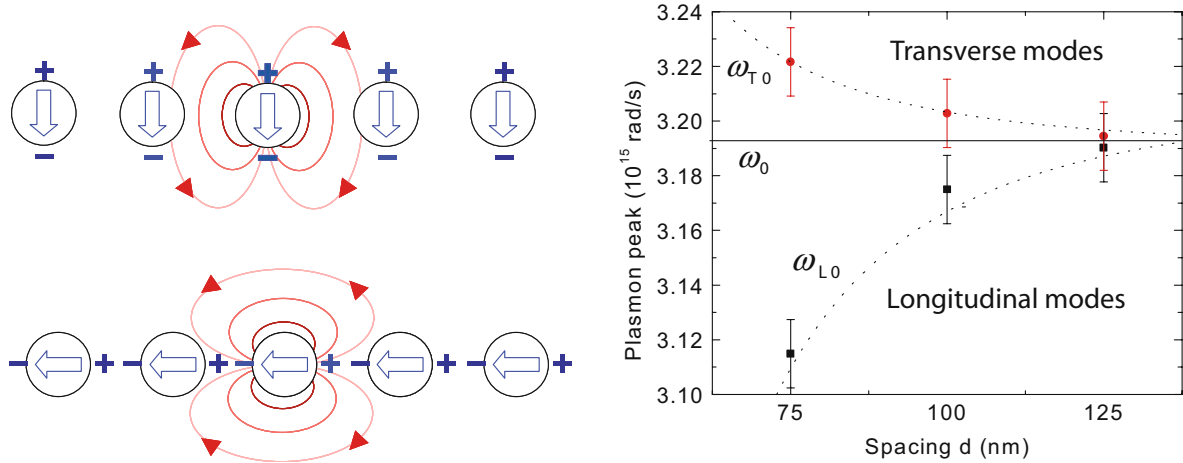


Figure 1.7: Experimental and theoretical plasmon coupling. Dipolar plasmons in chains of spherical AuNPs couple depending on field orientation [20] (left). Experimentally measured plasmon resonance energies in coupled AuNP chains show the gap-dependent tuning due to coupling [17] (right). The dotted line corresponds to a r^{-3} point dipole model.

in the metal with almost all field confined within a small lateral mode within the gap. This is known as a plasmonic ‘hot spot’. Through this mechanism alone the field enhancement $|E/E_0|$ can be increased by more than an order of magnitude. For this reason, attention has shifted from individual plasmonic nanostructures to coupled systems to extract the maximum performance.

Systems of AuNPs were experimentally studied from 2002 [17], in which the individual resonances of AuNP chains with different spacings were shown to couple and form two new modes gradually separating in energy with increased coupling strength (Figure 1.7). These modes are the in-phase coupled modes between particles in orthogonal polarisations. The resonance along the chain redshifts with increased coupling due to attraction between plasmons whereas the resonances perpendicular to the chain blueshift as dipolar plasmons in this orientation repel.

Interactions between plasmons appear similar to dipole-dipole interactions, which also depend on separation and relative orientation. Examples of some commonly considered dipole-dipole interaction geometries are shown in Figure 1.8. For two parallel dipoles aligned along their axes, driven in phase, the attractive coupling potential increases with decreasing separation, r , as $V \propto p_1 p_2 r^{-3}$ [21]. For an oscillating dipole this redshifts (decreases) the resonant frequency. Conversely, the repulsive interaction between two parallel dipoles positioned side by side also increases as r^{-3} , but blueshifts (increases) the resonant frequency. Symmetric anti-phase configurations lead to local field cancellation. Observation of such modes only becomes possible in non-symmetric dipole-dipole systems. Alternatively, for dimers outside of the quasistatic regime, phase retardation of the driving field across the dimer is capable of breaking the coupling symmetry, allowing these modes to be excited.

For plasmons in MNPs, the coupling interaction is well approximated using the dipole-dipole model [17, 22–25], however the restoring force within the particles also contributes to the potential and goes as the volume D^3 . The interaction energy between two plasmons therefore goes as $(r/D)^{-3}$. Since the gap size, $d = r - D$, is the defining feature of a plasmonic dimer, relations are often expressed in the quantity $(d/D) = (r/D) - 1$ rather than using the centre of mass separation. The resonant wavelength shift due to coupling can then be described using a plasmon ruler equation [26, 27],

$$\frac{\Delta\lambda}{\lambda_0} = a \exp\left(-\frac{(d/D)}{\tau}\right), \quad (1.46)$$

where a is the coupling strength and τ is a decay constant. The exponential decay is considered to be approximately equivalent to the $(d/D)^{-3}$ behaviour, which is expressed in terms of shape and size parameters, Λ and γ , as,

$$\frac{\Delta\lambda}{\lambda_0} = \frac{1}{12\Lambda(d/D + 1)^3 - (1 - \gamma)}. \quad (1.47)$$

In recent years this relation still shows good agreement with experimental data but the approach remains limited to describing only dipolar modes in simple geometries.

A slightly more complex model explaining the formation and behaviour of coupled modes was developed between 2003 and 2004. Plasmon hybridisation describes the plasmon resonances of a complex particle geometry by **deconstructing/decomposing** it into two simpler geometries [29, 30]. This is done in analogy with the ideas underpinning molecular orbital hybridisation and the hybridisation of quantum energy states. Using this logic, the theory equally describes the plasmon resonances of two coupled simple particle geometries [28] or a particle coupled with its image charge in a surface [31]. The multipolar modes of the individual dimer particles split in energy into two hybridised modes representing the bonding (in-phase) and anti-bonding (anti-phase) pole configurations. Due to the attractive and repulsive nature of the bonding and anti-bonding configurations the coupled modes redshift and blueshift from the initial mode position with decreasing separation, respectively. This behaviour is shown in Figure 1.9.

This model clearly shows that the bonding and anti-bonding modes have very different radiative properties. The bonding dipole exhibits a large net dipole moment due to parallel alignment of individual dipoles, whereas the anti-parallel aligned anti-bonding mode has no

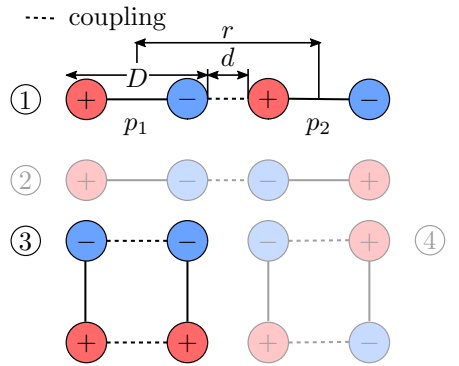


Figure 1.8: Diagram of dipole interactions. Dipoles have length D . The distance between dipoles is r with an edge-to-edge separation d . Configurations 1 and 3 are comparable with plasmon coupling as a result of sub-wavelength structures being driven by a single external light field. Configurations 2 and 4 are generally unphysical without significantly increasing the system size.

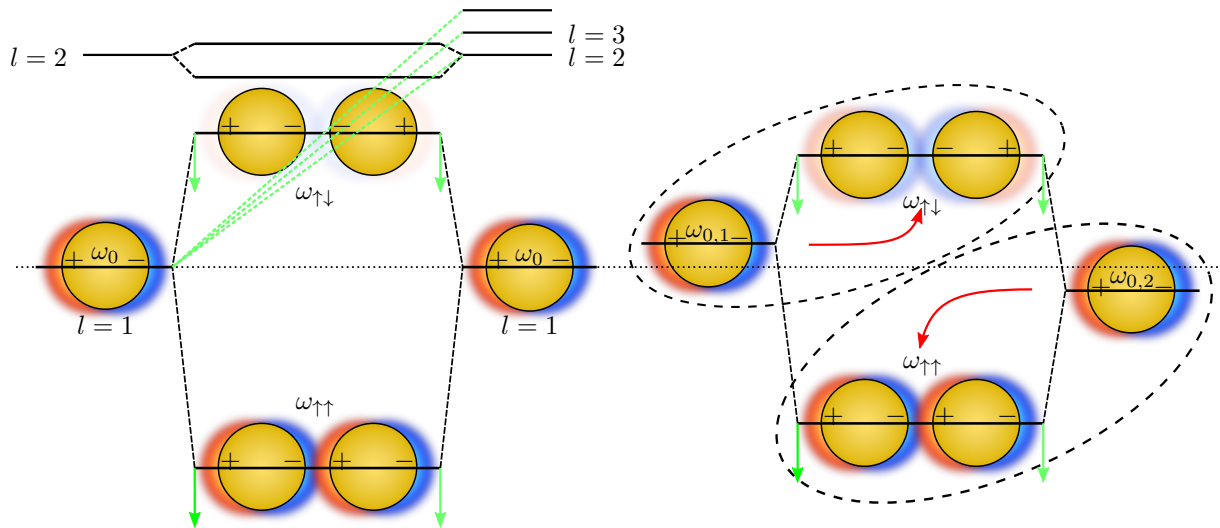


Figure 1.9: Diagram of plasmon hybridisation between coupled plasmons in a nanoparticle dimer. Plasmons are coupled along the dimer axis. Coupling leads to bonding and anti-bonding modes for each set of interacting l modes. Interaction with higher order l modes lowers the overall energy of lower order coupled modes (green lines). Only the bonding ($\omega_{\uparrow\uparrow}$) mode in the symmetric (homo-)dimer has a net dipole moment and is therefore observable. Cancellation of the net dipole moment means the anti-bonding ($\omega_{\uparrow\downarrow}$) mode remains optically dark. On the contrary, asymmetry in a (hetero-)dimer means both modes stay bright with the lower and higher energy individual modes forming the bonding and anti-bonding hybridised modes, respectively. This diagram is adapted from [28].

net dipole. As a result, the bonding mode strongly couples with light whereas the anti-bonding mode remains dark. Anti-bonding modes are consequently referred to as dark modes in symmetric systems. As stated earlier, should the mode acquire a finite net dipole, either through asymmetry of the dimer particles (difference material, size or shape) or phase retardation, it can become radiative and therefore experimentally observable. If this occurs then two resonances are observed upon coupling. The higher energy resonance blueshifts with decreasing separation to form the anti-bonding mode whilst the lower energy resonance redshifts and forms the bonding mode.

Hybridisation between two $l = i$ modes is also influenced by the presence of other modes of $l \neq i$, as is shown by the second set of dashed lines in Figure 1.9. For most simple dimer systems only the $l = 1$ mode is observed, however, with small gaps or large particles, higher order modes becomes observable. The $l = 1$ mode then experiences an increased rate of redshifting due to interaction with the appearing $l = 2$ mode **and so on**. Should the gap size become small enough, interaction between the redshifting bonding $l = 2$ mode and the blueshifting anti-bonding $l = 1$ mode can reverse the blueshift of the anti-bonding mode [28]. Classically, for nm-size gaps, a whole range of higher order modes are expected to exist in the

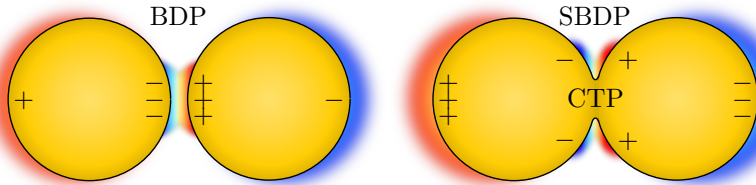


Figure 1.10: Diagram showing the emergence of charge transfer and screened bonding (crevice) plasmons on geometrical contact in a nanoparticle dimer. The field generated by the bonding dimer plasmon (BDP) is screened from the gap by the conductive contact, forcing capacitive coupling to the crevice gap in the form of the screened bonding dimer plasmon (SBDP). The dominant charge oscillation is then the charge transfer plasmon (CTP) through the conductive bridge and across the whole structure.

gap [32]. The lateral confinement of these modes across the gap is estimated using,

$$w = \sqrt{Rd}. \quad (1.48)$$

As with dipole coupling, an opposite effect occurs when the driving field is orientation perpendicular to the dimer axis. In this instance the excited plasmon poles repel each other more with decreasing separation and the bonding mode therefore blueshifts [33, 34].

1.2.2 The Dynamical Optical Response of Plasmonic Dimers: Transitioning from Capacitive to Conductive Plasmonic Coupling

Using modern numerical simulation techniques, the full separation-dependent optical response of a plasmonic dimer has been calculated as particles transition from non-interacting to hybridisation through to geometrical contact [32]. In these calculations, the lowest order plasmons hybridise, redshift and more intensely scatter as the separation decreases, with higher order modes eventually emerging. As the higher order modes become more intense, scattering from the lower order modes decreases. Despite this, their field enhancement continues to rise. These plasmons becoming so confined that they no longer couple with the far-field. This behaviour continues until the particles touch into geometrical contact.

Once in geometrical contact the gap becomes a conductive bridge. If it's length is small and it's conductance large, such that charge can be transported between particles within half an optical cycle, then charge transfer plasmons (CTPs) can form. The conductive short prevents the accumulation of surface charge on gap-facing metallic interfaces, reducing the capacitive coupling between plasmons (Figure 1.10). The bonding hybridised coupled modes are screened and forced outwards towards the crevice [32, 35, 36]. In another sense there are a finite number of electrons, each in a specific state, therefore if one electron transitions into a collective CTP oscillation then it's contribution is lost from it's original capacitive mode.

CTP modes, with their spatially larger dipoles, form at lower energies than the bonding

modes upon geometrical contact. As particles overlap, the dipole length decreases, increasing its energy, and CTPs resonances blueshift [32]. Each bonding mode has an associated CTP mode, corresponding to the screening and broadening of that mode's capacitive interaction since the gap conductivity σ and the local dielectric function $\varepsilon(\omega)$ are related.¹³ Greater overlap between particles widens the junction and increases the conductance, which, along with geometrical changes, strongly modifies the plasmonics. By lithographically creating overlapping discs it has been shown that the modes blueshift back to the single particle resonance upon complete overlap [25, 37].

The previously described effects can be broken down into a function of the contact geometry in the gap, where the gap between particles of radius R has a width d , conductivity σ with a conductive linker of radius a . Depending on these parameters there are two effects of a conductive linker - capacitive screening and charge transfer [35]. Screening occurs at low conductances once a contact has formed whereas excitation of a CTP requires a higher junction conductance. The conductance threshold for screening of the dipolar bonding plasmon is given by,

$$G_{\text{SBDP}} = \frac{\omega_{\text{BDP}}}{2\pi} \frac{a^2}{d}. \quad (1.49)$$

The threshold is intrinsically independent of geometry and depends only on the conductivity ($\sigma_{\text{SBDP}} = \omega_{\text{BDP}}/2\pi^2$). For larger contact widths or shorter linker lengths the threshold increases to overcome the increased capacitive coupling. A second threshold exists for CTP formation, occurring at,

$$G_{\text{CTP}} = \frac{\omega_{\text{CTP}}}{4\pi} \frac{R^2}{d}. \quad (1.50)$$

Similarly to G_{SBDP} , the conductivity threshold is expressed as $\sigma_{\text{CTP}} = (\omega_{\text{CTP}}/4\pi^2)(R/a)^2$. Unlike screening, CTP formation depends not only on the conductivity but the junction geometry. The geometry factor (R/a) represents the ratio between the total charge in the particle and the amount which can pass through a gap with fixed conductivity. Having a large conductivity means the junction does not have to be as wide, relative to the particle size, to accommodate enough current to maintain a CTP.

These results can be better understood in a number of limiting cases. For a fixed linked dimer geometry the optics can be controlled through the gap conductivity. Increasing the conductivity leads to screening, and therefore blueshifting, of the bonding mode before a CTP emerges [38, 39]. Since the geometry does not change the CTP, once excited, does not tune and the blueshift of the screened mode saturates. These systems have been experimentally realised using fractional mixing of conductive and insulating surface-assembled monolayers (SAMs), with results suggesting a $1G_0$ threshold to observe screening [40]. In the event that

¹³For a spherical MNP dimer with bonding hybridised dipolar (BDP) and quadrupolar (BQP) modes the corresponding CTP modes are typically labelled as CTP and CTP'.

the linker originates from the dimer metal, i.e. a AuNP dimer linked by a Au constriction, then the conductivity remains fixed and the width of the contact determines the extent of charge transfer. Under these conditions, screening occurs as expected and the CTP energy increases with linker width [38]. MNPs dimers fixed by hollow spacer molecules have exhibited this effect after high power laser pulses create Au threads of various widths [36, 41]. Dimers in which the gap width changes, leading to overlap, form the more complex system to understand since the geometrical changes also influence the plasmonics along with charge transfer.

This summarises the classical picture of plasmon coupling from capacitive to conductive coupling. However, the predictions of hybridisation theory break down at small, sub-nm gaps. Classical theory suggests that a continuum of higher order modes will be excited and redshift to a singularity as $d \rightarrow 0$, with the field enhancement increasing infinitely. This is completely unphysical behaviour and is rectified when quantum mechanics is considered. The classical picture description breaks down under two conditions - either the particles become sufficiently small that quantum non-locality and non-local effects (finite, non-negligible electron wavefunction spill-out from the particle) become important or the gap size decreases to scales on which quantum tunnelling can no longer be ignored. The onset of quantum tunnelling means charge is transported across the gap without requiring geometrical contact, rectifying the singularity predicted by classical electromagnetism.

The effects of quantum tunnelling were first predicted in small ($R < 2\text{ nm}$) NaNPs using full quantum mechanical, time-dependent density functional theory (DFT) calculations [43]. Since these calculations consider the behaviour of each electron, they are limited in complexity to small systems containing less than 2000 electrons. Tunnelling effects in larger metallic nanostructures are predicted by the quantum corrected model (QCM), a classical model which uses an effective gap dielectric function that takes into account the conductivity induced by quantum effects using pre-calculated values from DFT [42]. For large surfaces and small gaps the integrated contribution to conductance from tunnelling across the gap is enough to initially screen the bonding plasmons followed by the formation of CTPs (Figure 1.11). Screening leads to strong attenuation of the field enhancement in the gap. The lack of modes present when considering quantum effects is a result of electron tunnelling smoothing the effective junction surface. **Additionally, whilst the bonding mode appears to blueshift as a result of screening, simulations suggest that the blueshifting resonance is a higher order CTP excitation.**

Experimental evidence of quantum tunnelling influencing plasmon coupling has been observed using both optical spectroscopy [44, 46, 47], EELS [45], surface-enhanced Raman scattering (SERS) [47], photoluminescence [48] and third-harmonic generation measurements [49]. First measurements were made using optical scattering from a dynamic spherically-tipped Au AFM probe dimer, with simulated spectra using the QCM (Figure 1.12) [44]. Plasmon modes are shown to blueshift upon decreasing past a critical separation. Scattering spectra

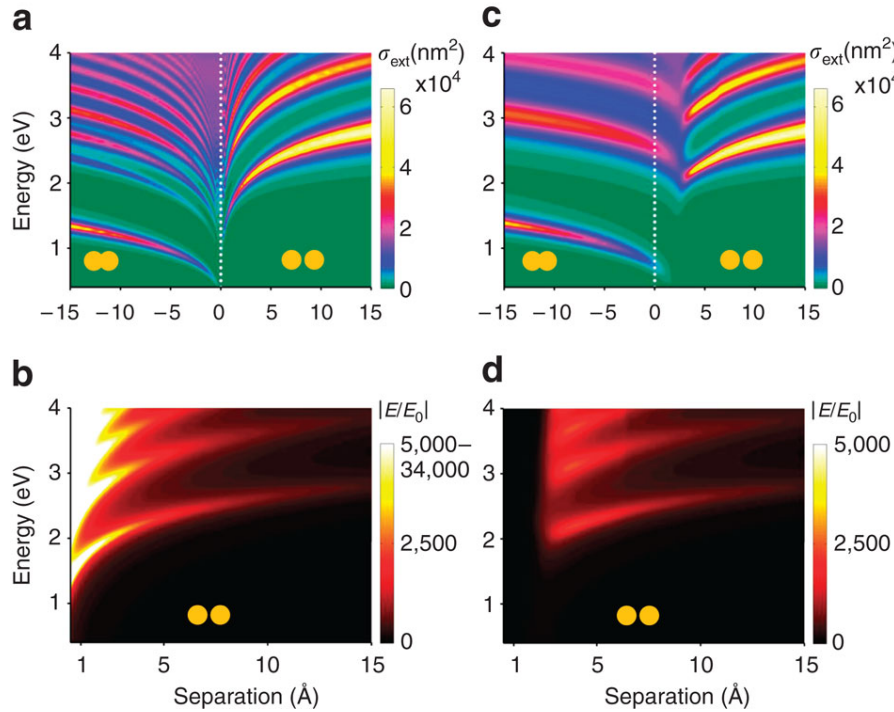


Figure 1.11: Numerical calculated extinction cross-section and field enhancement of a spherical AuNP dimer as a function of gap separation [42]. The classical approach (left), valid for separations greater than $\sim 5 \text{ \AA}$, shows many modes redshifting into a singularity on geometrical contact, following by blueshifting CTP modes as the particles overlap. Introduction of an effective (conductive) gap medium to emulate the effects of quantum tunnelling (quantum corrected model, right) demonstrate the early onset of screening and CTP formation prior to geometrical contact. Figure taken from [42].

qualitatively agreed with the QCM, with discrepancies attributed to difficulty in simulating an extended dual tip geometry. Better agreement with DFT calculations was found in EELS measurements on simpler 10 nm AgNP dimers, brought together under the influence of the electron beam (Figure 1.12) [45]. Alkanedithiol molecules of various lengths have also been used to discretely tune the gap separation of AuNP dimers [46]. In this case, blueshifting and attenuation of the bonding dipolar plasmon, as well as an increase in its width, is measured with molecules smaller than pentanedithiol. Similar results are found when using intercalating SAMs [50]. Further investigation into sub-nm plasmonic gaps have also shown changes attributed to quantum tunnelling, though inferred from properties depending on the gap field enhancement as opposed to direct measurement of the plasmon resonances. A decrease in signal intensity in both the SERS peaks [47] and photoluminescence [48] are signatures of quantum tunnelling screening the coupled plasmon field.

Interestingly, qualitative (and to some extent quantitative) agreement between QCM calculations and full quantum calculations suggest that the quantum nature of the system is of little importance. Despite only using a classical, resistive gap with conductances given by values characteristic of electron tunnelling, the effects of electron tunnelling on gap plasmons are

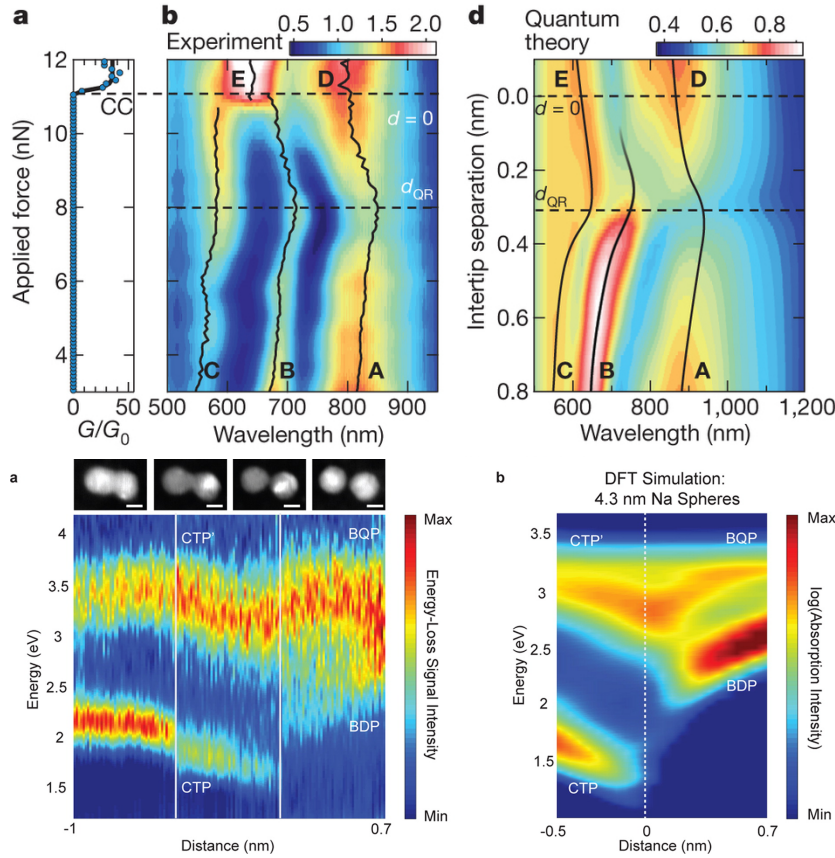


Figure 1.12: Examples of experimental measurements of the effect of quantum tunnelling on plasmonic gap systems through direct monitoring of the plasmon resonances. (top) Supercontinuum dark-field scattering measurements of two 300 nm diameter spherical Au tips in a dimer configuration with reducing separation, transitioning below 1 nm and into the quantum regime [44]. (bottom) EELS measurements of 10 nm AgNPs being induced closer together by the electron beam [45].

accurately replicated. This implies that, despite the quantum nature of electron tunnelling, its effects on plasmon coupling depend only on the amount of charge transfer and not the mechanism by which it occurs. This links together work done using particle positioning [44, 45] with studies of interacting plasmonic system coupled with molecular linkers [40, 46, 50]. Quantum tunnelling still remains an interesting case, however, since it is a form of conduction that is unavoidable once system sizes decrease below 0.5 nm. This is why its pinch-off point, the point at which the electric field in the gap is expelled, is described as the quantum limit to plasmon confinement [44]. It is for this reason why it is important to fully understand the relations between plasmonic hot spots and sites of (quantum) charge transfer.

Although charge transfer effects have been shown in previous reports by varying the conductivity of a fixed gap, there has yet to be a report showing the optical response of a dynamic dimer structure correlated with its electronic response. It is the aim of this project to successfully demonstrate and explain the possible ways in which electrical and optical plasmonic

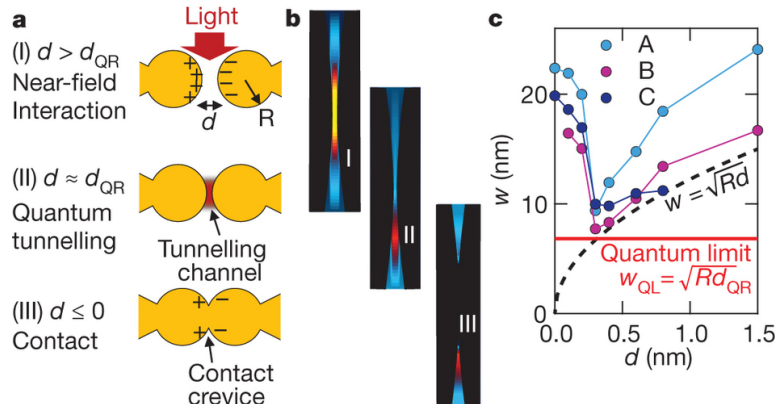


Figure 1.13: Plasmon mode distributions in the quantum regime. Diagram showing the different regimes of plasmonic interaction, taken from [44]. The onset of a tunnelling current pinches off the electric field in the gap via screening/conductive losses prior to conductive contact, which shows a similar expulsion of field from the gap.

phenomena intertwine/become entangled using a dual plasmonic nano-tip dimer. So far plasmons in planar and spherical/spheroidal geometries have been discussed, however many other geometries of metallic nanostructure support plasmons. Tips are one such geometry, currently receiving significant attention, that have been shown to support both SPPs and LSPs. In order to use nano-tips in determining the effects of quantum tunnelling on plasmonics, their supported plasmons must first be understood.

1.3 Plasmons in Tips

Significant efforts have been made to advance surface characterisation on the nm-scale by developing new optical tools and integrating optics into existing nanoscale topological measurements. Metallic tips were investigated due to the widespread use of scanning probe microscopies (SPMs), such as atomic force microscopy (AFM), and scanning tunnelling microscopy (STM). The similarity in size between metallic nanostructures and the small apex of tips initially suggested that visible plasmons would be expected, enabling resonant near-field enhancement. Prior to any spectral characterisation studies to understand the near-field response, tips were applied in combined SPM-optical microscopes to achieve sub-wavelength localisation and enhancement of optical signals. As the next logical step from SERS and scanning near-field optical microscopy (SNOM), the sharp apex of tips were exploited to develop the spin-off techniques of tip-enhanced Raman scattering (TERS) [51–54] and apertureless scanning near-field optical microscopy (a-SNOM)¹⁴ [55–60]. These are also known collectively as tip-enhanced near-field optical microscopy (TENOM).¹⁵

¹⁴Also known as scattering scanning near-field optical microscopy (s-SNOM).

¹⁵These are also sometimes known as field-enhancing near-field optical microscopy (FENOM) since apertured techniques do not necessarily exploit plasmonic enhancement as much.

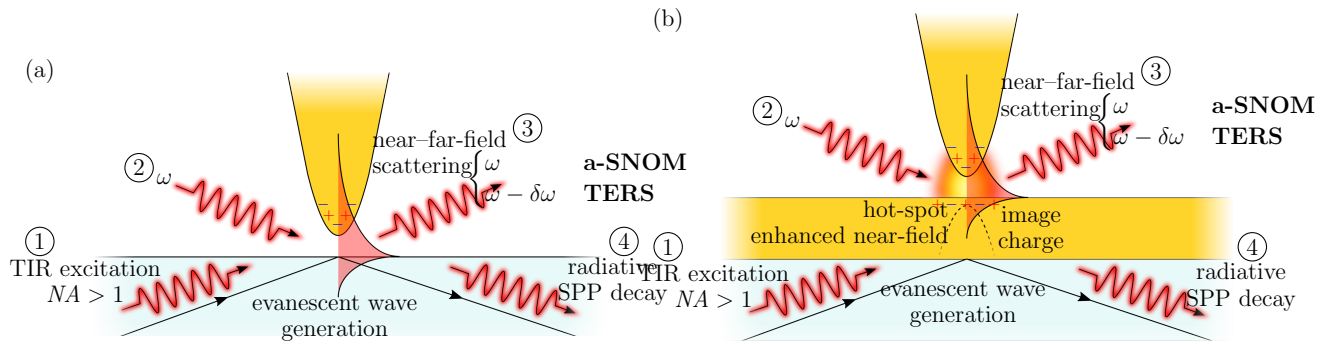


Figure 1.14: Concepts of TENOM. Basic TENOM systems constitute a tip and a sample (left). Tips can perturb evanescent surface waves, generated by high- NA TIR, and scatter them into the far-field (1 → 3) [63, 64]. Photons illuminating the tip can induce a weak dipole localised to the tip apex, which can scatter the near-field (2 → 3). More recent TENOM arrangements employ a metallic substrate to couple with the tip and further localise the field into a “hot spot” (right). Coupling of plasmons between the tip and the substrate can be achieved by exciting SPPs on the substrate using evanescent waves (1) or by focusing light on the MIM gap such that the tip dipole induces an image dipole in the substrate (2). Both mechanisms lead to scattering of light from the gap into the far-field (3). SPPs generated onto the planar surface (either via the tip or evanescent waves) can radiatively decay into $NA > 1$ (1, 2 → 4) [65].

The concept for TENOM was first proposed in 1985 [61] but it was not until 2000 that the first reported uses of tips for enhancing Raman spectroscopy emerged [51–54]. All measurements were carried out in inverted microscopes with either an AFM [51–53] or STM [54] mounted on top. Two of the initial measurements suggest the overall Raman enhancement has a lower limit of $\sim 10^4$ [51, 52], hence a field enhancement $\mathcal{O}(10)$, whereas a third obtained an enhancement factor of 80 from a single tip apex excited using $NA > 1$ evanescent waves, equivalent to the summed enhancement of many SERS hotspots on a Ag island film [53]. Since then Raman enhancements in the region of 10^7 – 10^9 have been measured [62].¹⁶ Whilst SERS enhancement factors have also increased significantly in recent years, the TENOM approach to spectroscopy remains a popular technique since the tip can be scanned across a sample. For this reason, techniques such as TERS are widely considered to become the successors of SERS. However, for this to be the case, nanotips require the capability to controllably and reproducibly enhance the near-field. Understanding the electromagnetic response of metallised tips has therefore become of significant importance in recent years. Since the use of tips for plasmonics is a central part of this project it is important to understand the underlying concepts and mechanisms of TENOM as these inevitably influence any observed plasmonic behaviour.

TENOM is ideally classified as a local excitation approach as opposed to a local scattering

¹⁶A clear distinction is made between the field enhancement, $|E/E_0|$, and the Raman enhancement, $|E/E_0|^4$, when stating enhancement factors. In the literature the terms “field enhancement” or “enhancement factor” are generally used interchangeably between the magnitude of the near-field and the improvement in the Raman signal.

approach [66], though the two approaches are not independent. Figure 1.14 shows the general approaches to TENOM. In the tip scattering approach the non-radiative near-field, comprising evanescent waves, is perturbed by the presence of the tip, leading to scattering into the far-field (**same frequency as illumination but lower k**). In the tip excitation approach the tip is resonantly excited to induce a large local near-field enhancement and used as a sub-diffraction-limited light source, from which the localised scattering can be measured. This process can be much more efficient than the pure scattering approach but depends on the optical antennae properties of the tip. In both cases the resolution of scattering images is sub-diffraction limited and on the order of the tip radius. In most cases this means a sub-50 nm resolution.

1.3.1 The Electromagnetic Response of Tips

The electromagnetic response of tips can be broken down into individual components that constitute the enhancement mechanism. The two main optical components are a lightning rod effect and a resonant plasmon contribution for metallic tips [67–69]. Each component is maximised when the incident field is along the tip axis [70]. The main focus of recent tip work has been to study the plasmonic component, however progress in sharpening tips has led to increases in the lightning rod component. Both components are important to consider when attempting to understand optical measurements involving tips.

Regardless of plasmonic behaviour, metallic tips intrinsically exhibit a lightning rod effect under the application of an applied field, instilling a non-resonant component of near-field enhancement. From the definition of the electric field $\mathbf{E}(\mathbf{r}) = -\nabla\varphi(\mathbf{r})$ it is clear that the electric field strongly depends on geometry, with field lines perpendicular to the equipotential conductor surface.

The more curved a surface, the more compressed the field lines become around its surface due to accumulation of surface charge. This can be described by $E = \sigma/\epsilon_0$ where $\sigma = q/4\pi r^2$ is the surface charge density and r is the radius of curvature. Since $E \propto 1/r^2$ the electric field is larger in regions of smaller curvature. This effect is shown using a simple sharp tip model in Figure 1.15. Consequently, even without a plasmonic component, sharp tips provide

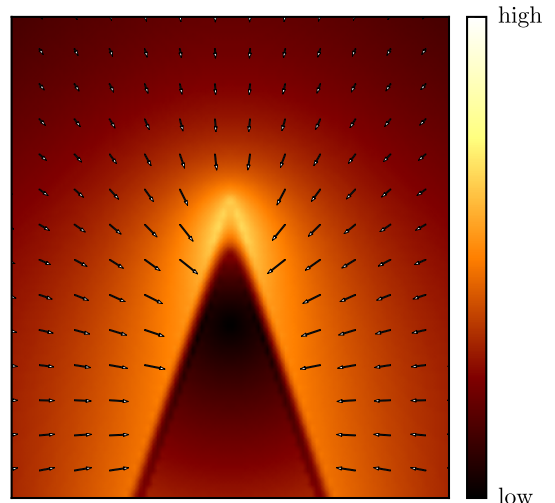


Figure 1.15: Calculated magnitude of the electric field around a tip showing the lightning rod effect. Compression of the field lines around the sharp corner of an equipotential surface leads to a localised, non-resonant field enhancement.^a

^aPoisson's/Laplace's equation is solved for a tip structured electrode with a surface charge distribution separated by some distance from a planar metal counter electrode of the opposite surface charge.

a promising platform for localised near-field enhancement.

The expected plasmonic component arises from the curvature of the metal-dielectric interface at the tip apex. This allows for either the excitation of SPPs at the apex or for SPPs propagating towards the apex to localise due to adiabatic nanofocussing [14, 71–75]. As highlighted when discussing ellipsoidal MNPs, strong, antenna-like LSPs are unlikely to be excited at the apex of a sharp tip since lack of a second metal-dielectric interface prevents accumulation of the opposite surface charge to the apex. The tip can almost be described as a MI geometry as opposed to the IMI geometry that results in antenna-like LSPs. Thus there can be no strong restoring forces or SPRs. The extended size of the typical tip structure ($\sim 20\text{ }\mu\text{m}$) also means that any potential low-order antenna modes would exist in the IR. Simulations of shorter tip geometries (nanocones or nanoellipsoids) show visible-NIR LSPs [76, 77], however these redshift and diminish with increasing tip length [68, 78]. The standard, sharp metallic tip geometry therefore makes for a poor *plasmonic* optical antenna unless SPPs can be excited.

Despite this claim, a large number of publications give convincing evidence for the presence of localised apex plasmons, such as TERS background resonances [79, 80] and depolarised scattering images [81], however these typically have a degree of nanostructuring capable of sustaining more localised modes [81–84]. These localised components of the plasmonic tip contribution are generally reported to originate from surface roughness imparted by the coating procedure that mimics small 10–50 nm MNPs [81]. Similar behaviour has been used to explain the origin of SERS in rough metal films. Each grain of the coating acts as a point at which photons couple or plasmons radiate, hence a grain located at the apex can plasmonically enhance the near-field. For this reason sharp tips are generally all solid etched metal or metallised dielectric tips, coated using evaporation (with similar conditions to metal island deposition) [81, 82, 84] or chemical reactions [83].

In general there is the consensus that tips, in some way, support both SPPs and LSPs, which, under different conditions, contribute to the overall near-field enhancement with differing degrees of magnitude. More work is needed to fully understand and optimise the tip geometry to gain the most from enhancement. Alternatively the tip is coupled with a planar metallic substrate to effectively form a plasmonic MIM cavity, enabling localised gap modes [75, 80, 85–89]. In this instance, a weakly-excited dipole in the tip can induce an image dipole in the metallic surface to form a strongly-confined coupled mode in the gap. Coupling can be achieved either by exciting the tip dipole or by using SPP excitation on the underlying metallic substrate [87]. Unlike the coupling between MNP plasmons, theory suggests that the coupling between a Au tip and a Au surface only minimally shifts the gap resonance [90].

Complete understanding of these effects from theory is challenging due to the difficulty in modelling tips. The small sub-wavelength apex structures but overall large conical or pyramidal tip structure, extending over $20\text{ }\mu\text{m}$, cause issues leading to many physical inaccuracies.

Some of these include unphysical modes caused by interference of reflected SPPs around the tip surface. Incredibly simplistic models, such as modelling only the tip apex, usually as a spherical or ellipsoidal MNP, fail to take into account the actual tip geometry, resulting in the existence of unphysical MNP-like modes at the tip apex. Similar multipolar modes are exhibited by tip models with finite lengths less than 1 μm [76, 77], behaving more like nanopyramids [91, 92]. Realistic excitation of geometrical (spherical) LSP resonances at the apex, similar to those in MNPs, have weak dipole moments as a result of the singular metal-dielectric interface and are therefore far less radiative than MNPs [90]. **The lack of radiative lower order multipolar resonances greatly diminishes the radiative cross section [93]**. Recent models accounting for the actual tip length show the disappearance of such modes into a smooth continuum as the tip is continually lengthened [68].

Zhang *et al.* suggest that between lengths of 200 nm and infinity a tip transitions between supporting low order LSPs, then higher order LSPs, followed by only weak SPPs. LSPs are supported only when the entire tip structure is comparable in size to the focus, allowing light to drive in-phase collective oscillations of the conduction electrons. As the tip becomes larger than the focus, and hence the illumination wavelength, phase retardation occurs and higher order LSP modes dominate. Once the tip becomes larger than the focus, the case for almost all SPM-based tips, collective oscillations are no longer possible, leaving only LSPs concentrated at the apex surface and SPPs. SPPs form the periodic response in the field enhancement before disappearing due to increased losses with increasing tip length. The field enhancement then rises smoothly and non-resonantly towards the IR as only a lightning rod contribution remains and the relative apex sharpness compared to the illumination field increases with wavelength. Interestingly, Zhang *et al.* further show that a sharp tip with a 10 nm radius cannot compete with the enhancements brought on by collective LSP excitation in a broader radius structure.

Even with the current frequent use of TENOM there has been little experimental work reported on the direct measurement of the optical response of tips or characterising their spectra prior to use, for example, in TERS. The first direct observation of plasmons in tips was in 2005. Scattering of evanescent waves at the surface of a prism by a tip was used to measure the near-field response in Au tips [63]. The 600–800 nm spectral resonance present in Au, but not W, was attributed to excitation of SPPs at the tip apex. Two separable *s* and *p*-polarised modes were extracted from the plasmonic Au spectra showing the expected anisotropy along each of the tip axes. Further independent measurements of evanescent field scattering have shown similar results [64, 94]. Shifts of \sim 75–100 nm were observed between Ag and Au tips with a Si_3N_4 base tip redshifting tip resonances \sim 30 nm compared with coated W tips. This dependence on tip structure has been highlighted numerous times due to the two dominant tip geometries of sharply etched metal tips and metallised (metal-coated)

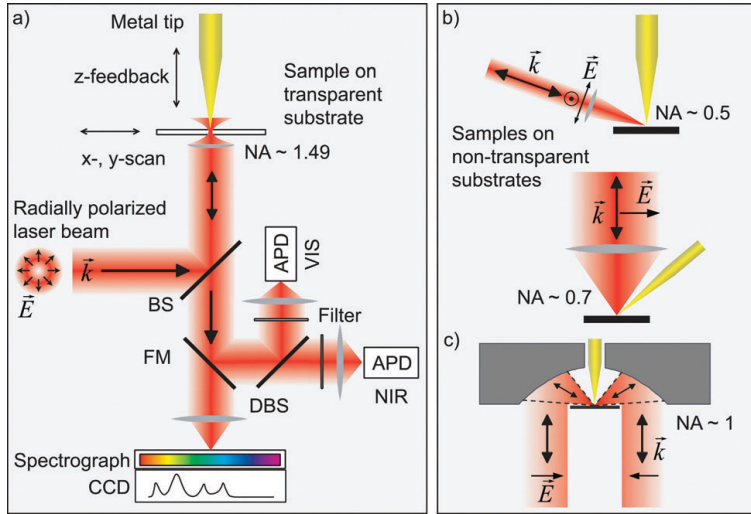


Figure 1.16: Typical optical geometries found in TENOM experiments [95]. The most prominent system is the bottom-illumination/back-illumination configuration utilising high-NA objectives. The other main geometry is the side-illumination configuration.

non-metallic tips.

1.3.2 Challenges associated with Tip-based Near-Field Microscopy

Since initial investigations, tip-based systems have been designed in two configurations: the side-illumination configuration and the bottom-illumination configuration. Both configurations are shown in Figure 1.16. The specific design of a TENOM microscope is important as it defines the collection and, more importantly, excitation geometries for the tip. Side-illumination has been used successfully in a number of cases [64, 96, 97] but suffers generally from far-field scattering overshadowing the near-field scatter. This requires more complex optical geometries to overcome, such as using polarisation-resolved or interferometric approaches. More recent designs have opted for a side-illumination geometry, in which high NA is achievable by using parabolic reflectors instead of an objective lens [98].

The dominant microscope design is the bottom-illumination configuration using a $NA > 1$ objective to illuminate the tip evanescently whilst masking out the $NA < 1$ illumination in k -space. Total internal reflection (TIR) of the incident light results in minimal background scatter with only the near-field scattered into a collection aperture. Collection from this geometry can be achieved using either the $NA < 1$ aperture of the high NA objective [81, 82, 99–102] or a secondary low NA objective [87, 89, 103]. More importantly, bottom-illumination is advantageous in that it generates evanescent waves capable of coupling to SPPs in both a metallic substrate and the tip once it is within the near-field. The disadvantage of using bottom-illumination is that it requires semi-transparent samples (enough to transmit and collect sufficient light), which is not always possible. In general each of these setups is used

with a continuous wave laser, although recently ultrafast systems have been employed to extract temporal information from TERS measurements [104].

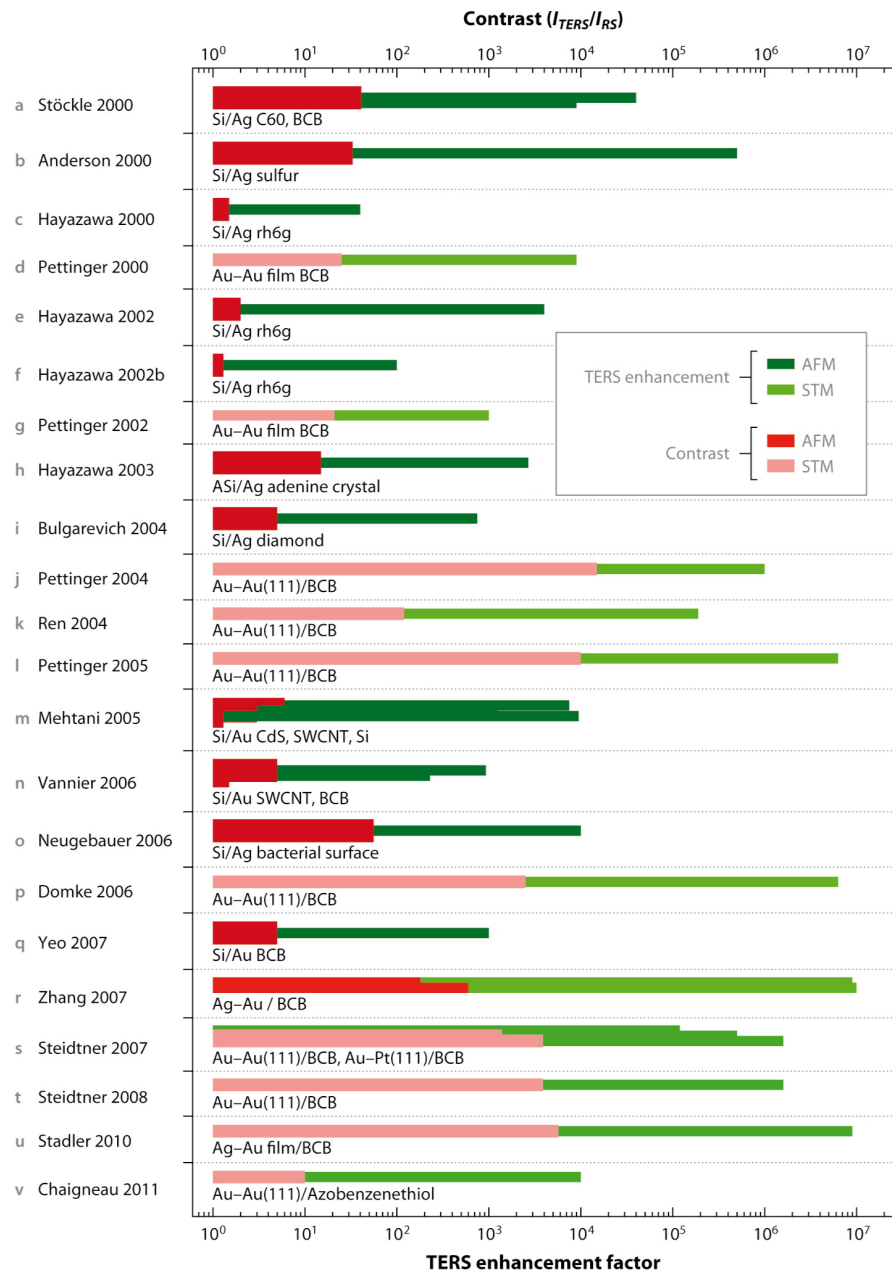
Since the initial measurements of tip enhancements and plasmons, techniques such as TERS and a-SNOM have become widespread and generally accepted. However, they are currently not reliable enough to be considered as a standard technique. Difficulty controlling the tip near-field is both a result of the irreproducibility of the tip geometry and a lack of understanding of the optical processes governing the enhancement, leading to large variations between reported field enhancements. A selection of TERS field enhancements and contrasts from reports between 2000 and 2011 showing the large variability are shown in Figure 1.17. The current challenges with TENOM are therefore improving the reproducibility of the near-field enhancement between tips [81, 102, 105] and successful electromagnetic modelling and understanding of the tips themselves [].

From Figure 1.17 it is clear that sharper STM tips result in larger field enhancements than AFM tips and comparative studies have shown similar trends [99, 106, 107]. This is most likely evidence that the lightning rod effect plays a significant role in the near-field enhancement process. Intuition suggests that the sharper profile of solid metallic STM tips means a larger lightning rod component compared with metallised AFM tips, a hypothesis also suggested in recent theory work [68]. Theory further suggests that there is a quantum limit in sharpness, set by nonlocal effects, before the field enhancement saturates as field localisation at structural imperfections becomes smoothed [108]. Studies have also shown that some large observed enhancement factors can be caused by non-plasmonic artefacts from the tip shaft [109]. Removal of these artefacts is necessary to recover the actual near-field enhancement [102].

Variability between similar measurements is not solely due to differences in experimental setup or changes in tip sharpness. A large amount of variability stems from the surface metal morphology. The disadvantage of relying on LSP excitation at a roughened apex is that the randomised tip geometry is not reproducible. Furthermore, granularity is rarely taken into account in theory when trying to explain the mechanisms of TENOM. The orientation of the tip, as well as the orientation of the roughened apex, with respect to the sample and the incident excitation field has also been known to influence the near-field enhancement [81, 99]. It is the limitations imposed by the reproducibility of this complete plasmonic geometry that mostly restrict the progress of TENOM.

As with much of plasmonics, material dependence is a factor which strongly determines the localisation of light. As with conventional plasmonic structures, Ag tips generally outperform Au tips under visible light, though these claims are highly dependent on the underlying tip material and the morphology of the metallic surface used in the experiment. Plasmon excitation is complicated by the shift induced by refractive index of the underlying tip material

Figure 1.17: Comparison of TERS field enhancements and contrasts reported between 2000 and 2011 [62]. STM tips, likely due to their increased sharpness, outperform AFM tips. Ag tips outperform Au tips. Larger enhancements are observed in systems where there is an underlying thin, noble metallic film. Statistical correlations still remain somewhat weak, showing the current variability in TERS experiments, attributed to irreproducibility of enhancing tips.



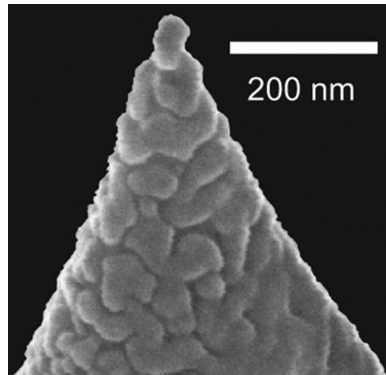


Figure 1.18: SEM images of metallised tips showing the granular texture and apex sharpness. (a)[81, 82, 84].

in metallised AFM tips, which can vary drastically between materials such as Si, SiO_2 , and Si_3N_4 [103, 107]. These high index materials can shift SPRs into the infrared (**IMI plasmon geometry**) whereas plasmons in solid metal STM tips remain unchanged. This forms another partial explanation for the better enhancements seen with STM tips. Careful consideration must therefore be given when pairing a tip with a laser in order to match the excitation wavelength with the SPR [84, 99, 100, 110]. Numerical simulations further show that resonance positions are highly sensitive to the metallic coating thickness when below the skin depth (~ 40 nm for Au), suggesting some experimental variability originates from uncertainties in the metallic deposition process [78].

Larger enhancements have resulted from coupling with thin metallic substrate films, suggesting the formation of gap plasmons [80, 85, 87–89]. Specifically, when a Au tip is paired with a Au substrate the field enhancement is significant increased, moreso than when paired with a Pt surface [85] or a non-metallic surface [90] due to better optical polarisability of the substrate. In these cases the Raman enhancement has been shown to rise to $\sim 10^7$ – 10^9 when illumination is on resonance with the gap mode [89].

Finally, variability between similar measurements can stem simply from differences in tip placement, optical setup and the specific illumination/collection geometry or optics used. As tips are rarely characterised there is little traceability between measurements from which to systematically determine the relevant causes for difference.

One final tip-based plasmon excitation mechanism of interest that has been discussed in recent years is electrical excitation. Similar to the use of EELS in electron microscopy, tunnelling electrons can be used to excite plasmons in an STM geometry. Since tips are typically illuminated with a single wavelength of light it becomes difficult to discern plasmonic features hidden in the collected light. Electrical excitation circumvents this limitation as electrons need only to have sufficient energy eV that a portion transferred to the conduction electrons is enough to excite SPs with frequencies $h\nu \leq eV$. Electrical excitation also functions

to both remove background light contributions to spectra by removing the illumination source.

Using tunnelling current excitation, light has been observed from both the tip-air-metal substrate gap [79, 80] and the interface between the metal substrate and its underlying dielectric [65]. Broad resonances, which redshift with decreasing tip-sample separation, are found superimposed onto TERS spectra when operating in the STM configuration [79, 80]. These suggest the formation of a MIM gap mode. Light detected from metal-glass interfaces is leakage radiation from SPPs on the metal-air interface. Since light cannot leak from SPPs at the metal-air interface the detected light must be scattering from gap plasmons between the tip apex and the surface **and outcoupling at the curved surface**. It is thought that 95% of the emission is due to SPP excitation rather than LSP excitation [65].

1.3.3 Tip Modification, Nanostructuring and Optical Antenna Tips

The mode mismatch caused by the size difference between diffraction-limited light and the nm-scale results in a 3–4 order of magnitude coupling efficiency loss [73]. As described previously, a SP acts as an optical antenna. A good optical antenna has the ability to effectively modify the density of electromagnetic states such that the far-field radiation impedance is efficiently matched with the impedance of a near-field evanescent mode and vice versa [66, 111]. The antenna opens up scattering pathways between near-field emitters and the far-field by connecting wave states (k -vectors) via new intermediate states (the plasmon). As stated previously, sharp metallic tips, in their standard form, are not particularly good optical antennae. To improve their coupling efficiency, standard sharp tips and their surrounding structures can be modified or nanostructured to introduce such intermediary plasmon states which couple the far-field to the near-field [95]. Whilst the most basic method of achieving this is by roughening the metal surface, more reliable and reproducible methods have been developed to controllably nanostructure the tip and potentially introduce better antenna behaviour.

By patterning a grating onto the side of a conical metallic tip, its apex can be transformed into a nanoscale light source, in which SPPs excited on the grating propagate to the apex and re-radiate into the near-field [112]. Far-field illumination remains spatially separated from the apex suppressing far-field background scatter allowing only near-field scattering from the apex to be measured. The conditions for adiabatic nanofocussing mean that only a single SPP mode will localise at the apex and radiate. Background-free TERS signals using the resulting 10 nm light source at $\lambda = 800$ nm, excited both with continuous wave and ultrafast lasers, have been detected to demonstrate the benefits of using SPPs to spatially separate the near-field and far-field scatter [14, 73].

Recently, nanostructuring of the tip apex has been investigated in order to tune and optimise the plasmonic antennae properties of nanotips. Through nanostructuring new plasmon modes unsupported by regular sharp tips can emerge, opening up new mechanisms by which

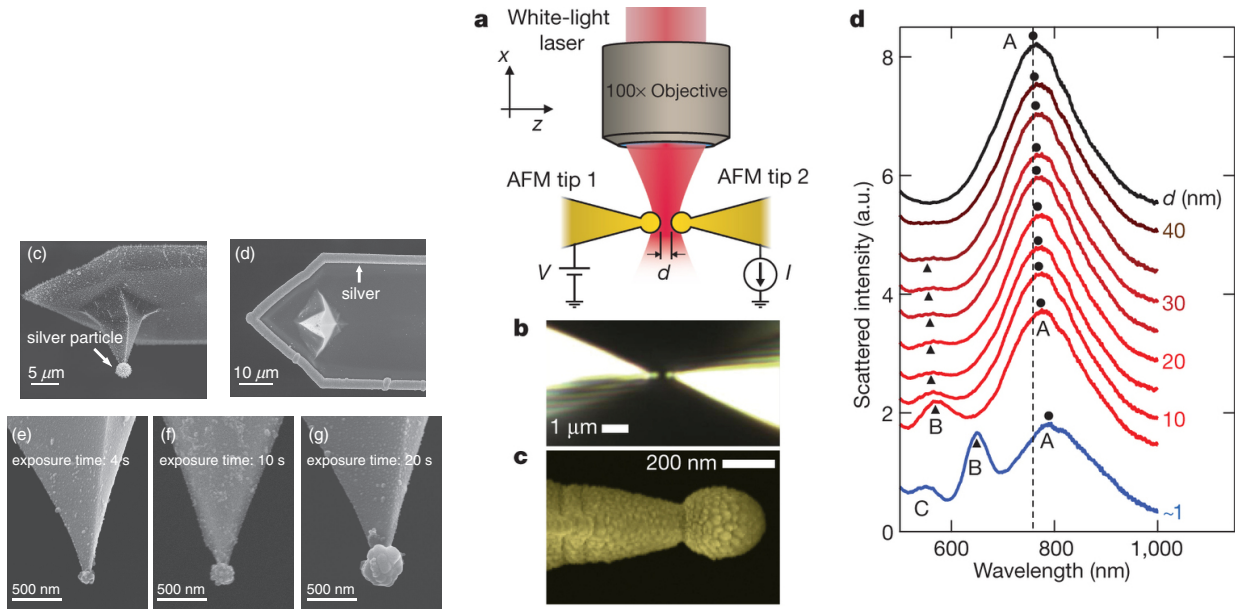
light can be channelled to the nm-scale, such as direct far-field illumination. To create the necessary LSP antenna states for efficient plasmon coupling in the visible spectrum tips must be structured with distinct, sub-wavelength sized metallic features.

Nanostructuring tips with other geometries has led to an order of magnitude increase in field enhancement, attributed to LSP excitation [113]. Electrochemical etching [114], FIB machining [115], selective deposition [116] and nanostructure grafting [117] have successfully been used to create nanotips which are good optical antennae, especially when illuminated on resonance. Scattering resonances have been directly measured on a subset of these tips [115, 116] while others use the field enhancement at common laser wavelengths as a measurement of antenna quality [114, 117].

Designs in which the tip is removed and replaced with a planar bow-tie antenna [118] or nano-cone [119] have successfully demonstrated improved field enhancement attributed to excitation of a SPR at the apex. Lack of a strong plasmonic contribution from sharp Au metallised tips to TENOM is further evident from direct comparison with Au nanotip probes. A Si tip with the apex replaced by a Au nanotip outperforms a standard Au AFM tip by 120% in the side illumination geometry [117]. Similarly cutting the Au coating off past the apex also enables LSPs [116]. This level of modification is carried out using FIB machining and is therefore highly controllable, though at the cost of fabrication time and expenses. Similar structures exhibiting SPPs for improved TENOM have also been made by etching tips [114, 120], NP pickup [121] and various other methods. However, to date there are very few reported methods of simply nanostructuring a tip without the need for FIB, electron microscopy or complex chemistry. A significant amount of time on this project was therefore spent determining a simple approach for chemically producing plasmonic tips. The targeted geometry of choice was the spherical tip apex.

The simplest geometry to impart onto a tip apex is a sub-wavelength metal sphere. By doing so the tip gains LSPs similar to those in an isolated spherical MNP. The specific SPRs depend on the sphere attachment method as the base tip structure determines the local dielectric medium adjacent to the MNP. SPRs have been observed in the far-field [44], with coupling between plasmons used to confirm plasmonic behaviour. Additionally, a $20\times$ increase in field enhancement has been measured when using a photochemically-fabricated spherical AgNP-on-Pt tip compared with a sharp Ag tip [113]. The increase in field enhancement also comes with an increase in **resolution/spatial localisation**.

Other than their successful application in TERS and fundamental plasmonics studies, the origin of SPRs in spherical tips has not yet been fully investigated. To date there has been very little work done to reliably produce and characterise the optics of spherically nanostructured tips. Furthermore, there is still work needed to similarly measure the optical response of sharp tips, comparing them directly and quantitatively with nanostructured tips. A large part of



(a) Photochemically fabricated AgNP-on-Si tips for TERS [113]. Field enhancement is increased $\sim 20\times$ compared with sharp Ag tips when using 488 nm illumination with a 1.4 NA objective in an inverted microscope.

(b) Experimental evidence of spherical tip plasmons and their dynamic coupling into the quantum regime of plasmonics [44]. Spherical tips are Au-coated NanoTools B150 AFM probes (150 nm radius of curvature), selected to minimise sensitivity to axial tip-tip alignment, to increase the scattered signal levels, and support higher-order plasmonic cavity modes in the visible spectrum. Resonances are far-field excited using a supercontinuum laser source in a side-illumination configuration. Separation-dependent coupling between two spherical tips confirms plasmonic behaviour.

Figure 1.19: Examples of spherical tip fabrication and surface plasmon resonances.

this project focusses on the development of a simple method for producing plasmonic tips with understood far-field optical responses. The comparison with sharp metallic tips can then be made and plasmonic tips applied in both fundamental studies and near-field enhancement.

1.4 Conclusions

Charge transfer effects in plasmonic systems are a phenomenon still requiring significant investigation. The influence of electron tunnelling has only been touched upon in recent years. Tips, if possessing far-field antenna plasmons, provide a useful platform for studying fundamental plasmonics in a dynamic way. Their well-developed experimental geometries for topological measurements form the basis of microscopes integrating optics and tips. By using such a setup the quantum regime of tunnelling plasmonics can be further investigated.

To date there has been no direct correlated measurements between plasmon resonances and quantum tunnelling. Tunnelling has been inferred from direct measurements of plasmon

resonances without electronic measurements [44, 45] and from variables influenced by the gap field enhancement, though in some cases with electronic measurements [46, 47, 49, 50]. The effects of tunnelling, specifically the relations between screening and CTP excitation, can be better understood with correlated electrical and force measurements. By using an experimental geometry related to AFM these measurements become possible.

References

- [1] J. C. Maxwell, Philosophical Transactions of the Royal Society of London, 459–512 (1865).
- [2] P. Drude, Annalen der Physik **306**, 566–613 (1900).
- [3] P. B. Johnson and R.-W. Christy, Physical Review B **6**, 4370 (1972).
- [4] R. Egerton, *Electron energy-loss spectroscopy in the electron microscope* (Springer Science & Business Media, 2011).
- [5] A. Otto, Zeitschrift für Physik **216**, 398–410 (1968).
- [6] E. Kretschmann, Zeitschrift für Physik **241**, 313–324 (1971).
- [7] R. Wood, The London, Edinburgh, and Dublin Philosophical Magazine and Journal of Science **4**, 396–402 (1902).
- [8] U Fano, JOSA **31**, 213–222 (1941).
- [9] W. A. Murray and W. L. Barnes, Advanced materials **19**, 3771–3782 (2007).
- [10] J. D. Jackson, *Classical electrodynamics* (John Wiley & Sons, 1999).
- [11] J. Mock et al., The Journal of Chemical Physics **116**, 6755–6759 (2002).
- [12] H. Kuwata et al., Applied physics letters **83**, 4625–4627 (2003).
- [13] C. F. Bohren and D. R. Huffman, *Absorption and scattering of light by small particles* (John Wiley & Sons, 2008).
- [14] S. Berweger et al., The Journal of Physical Chemistry Letters **3**, 945–952 (2012).
- [15] G. Mie, Annalen der physik **330**, 377–445 (1908).
- [16] J. Krenn et al., Applied Physics Letters **77**, 3379–3381 (2000).
- [17] S. A. Maier, P. G. Kik, and H. A. Atwater, Applied Physics Letters **81**, 1714–1716 (2002).
- [18] J. Mertens et al., Nano letters **13**, 5033–5038 (2013).
- [19] B. de Nijs et al., Faraday Discussions (2014).
- [20] S. A. Maier, *Plasmonics: fundamentals and applications* (Springer Science & Business Media, 2007).
- [21] N. J. Halas et al., Chemical reviews **111**, 3913–3961 (2011).
- [22] U. Kreibig and M. Vollmer, *Optical properties of metal clusters*, Vol. 25 (Springer Berlin, 1995).

- [23] M. Gluodenis and C. A. Foss, *The Journal of Physical Chemistry B* **106**, 9484–9489 (2002).
- [24] W Rechberger et al., *Optics Communications* **220**, 137–141 (2003).
- [25] T. Atay, J.-H. Song, and A. V. Nurmikko, *Nano Letters* **4**, 1627–1631 (2004).
- [26] P. K. Jain, W. Huang, and M. A. El-Sayed, *Nano Letters* **7**, 2080–2088 (2007).
- [27] X. Ben and H. S. Park, *The Journal of Physical Chemistry C* **115**, 15915–15926 (2011).
- [28] P. Nordlander et al., *Nano Letters* **4**, 899–903 (2004).
- [29] E Prodan et al., *Science* **302**, 419–422 (2003).
- [30] E Prodan and P. Nordlander, *The Journal of chemical physics* **120**, 5444–5454 (2004).
- [31] P. Nordlander and E. Prodan, *Nano Letters* **4**, 2209–2213 (2004).
- [32] I. Romero et al., *Optics Express* **14**, 9988–9999 (2006).
- [33] L. Gunnarsson et al., *The Journal of Physical Chemistry B* **109**, 1079–1087 (2005).
- [34] S.-C. Yang et al., *Nano letters* **10**, 632–637 (2010).
- [35] O Pérez-González et al., *Nano letters* **10**, 3090–3095 (2010).
- [36] C. Tserkezis et al., *Optics express* **22**, 23851–23860 (2014).
- [37] J. B. Lassiter et al., *Nano letters* **8**, 1212–1218 (2008).
- [38] O Pérez-González, N Zabala, and J Aizpurua, *New Journal of Physics* **13**, 083013 (2011).
- [39] N. Zabala et al., in *Spie nanoscience+ engineering* (International Society for Optics and Photonics, 2011), pp. 80961L–80961L.
- [40] F. Benz et al., *Nano letters* (2014).
- [41] L. O. Herrmann et al., *Nature communications* **5** (2014).
- [42] R. Esteban et al., *Nature Communications* **3**, 825 (2012).
- [43] J. Zuloaga, E. Prodan, and P. Nordlander, *Nano letters* **9**, 887–891 (2009).
- [44] K. J. Savage et al., *Nature* **491**, 574–577 (2012).
- [45] J. A. Scholl et al., *Nano letters* **13**, 564–569 (2013).
- [46] H. Cha, J. H. Yoon, and S. Yoon, *ACS nano* **8**, 8554–8563 (2014).
- [47] W. Zhu and K. B. Crozier, *Nature communications* **5** (2014).
- [48] V. Kravtsov et al., *Nano letters* **14**, 5270–5275 (2014).
- [49] G. Hajisalem, M. S. Nezami, and R. Gordon, *Nano letters* **14**, 6651–6654 (2014).
- [50] S. F. Tan et al., *Science* **343**, 1496–1499 (2014).
- [51] R. M. Stöckle et al., *Chemical Physics Letters* **318**, 131–136 (2000).
- [52] M. S. Anderson, *Applied Physics Letters* **76**, 3130–3132 (2000).
- [53] N. Hayazawa et al., *Optics Communications* **183**, 333–336 (2000).
- [54] B. Pettinger et al., *Electrochemistry* **68**, 942–949 (2000).

- [55] F Zenhausern, M. O'boyle, and H. Wickramasinghe, *Applied Physics Letters* **65**, 1623–1625 (1994).
- [56] F. Zenhausern, Y Martin, and H. Wickramasinghe, *Science* **269**, 1083–1085 (1995).
- [57] R Bachelot, P Gleyzes, and A. Boccara, *Optics letters* **20**, 1924–1926 (1995).
- [58] B Knoll et al., *Applied physics letters* **70**, 2667–2669 (1997).
- [59] B Knoll and F Keilmann, *Applied Physics A: Materials Science & Processing* **66**, 477–481 (1998).
- [60] F Keilmann, B Knoll, and A Kramer, *physica status solidi (b)* **215**, 849–854 (1999).
- [61] J. Wessel, *JOSA B* **2**, 1538–1541 (1985).
- [62] B. Pettinger et al., *Annual review of physical chemistry* **63**, 379–399 (2012).
- [63] C. Neacsu, G. Steudle, and M. Raschke, *Applied Physics B* **80**, 295–300 (2005).
- [64] D Mehtani et al., *Journal of Optics A: Pure and Applied Optics* **8**, S183 (2006).
- [65] T Wang et al., *Nanotechnology* **22**, 175201 (2011).
- [66] L. Novotny and S. J. Stranick, *Annu. Rev. Phys. Chem.* **57**, 303–331 (2006).
- [67] R Esteban, R Vogelgesang, and K Kern, *Nanotechnology* **17**, 475 (2006).
- [68] W. Zhang, X. Cui, and O. J. Martin, *Journal of Raman Spectroscopy* **40**, 1338–1342 (2009).
- [69] T. Schmid et al., *Angewandte Chemie International Edition* **52**, 5940–5954 (2013).
- [70] M Zhang, J Wang, and Q Tian, *Optics Communications* **315**, 164–167 (2014).
- [71] M. I. Stockman, *Physical review letters* **93**, 137404 (2004).
- [72] D. Pile and D. K. Gramotnev, *Applied Physics Letters* **89**, 041111 (2006).
- [73] S. Berweger et al., *The Journal of Physical Chemistry Letters* **1**, 3427–3432 (2010).
- [74] J. S. Lee et al., *Optics express* **19**, 12342–12347 (2011).
- [75] N. C. Lindquist et al., *Laser & Photonics Reviews* **7**, 453–477 (2013).
- [76] R. M. Roth et al., *Optics Express* **14**, 2921–2931 (2006).
- [77] A. Goncharenko et al., *Applied physics letters* **88**, 104101 (2006).
- [78] C. Huber et al., *Physical Chemistry Chemical Physics* **16**, 2289–2296 (2014).
- [79] B. Pettinger et al., *Physical Review B* **76**, 113409 (2007).
- [80] B. Pettinger et al., *Surface Science* **603**, 1335–1341 (2009).
- [81] T. Mino, Y. Saito, and P. Verma, *ACS nano* **8**, 10187–10195 (2014).
- [82] N. Hayazawa et al., *Chemical Physics Letters* **335**, 369–374 (2001).
- [83] E. Bailo and V. Deckert, *Chemical Society Reviews* **37**, 921–930 (2008).
- [84] N. Hayazawa, T.-a. Yano, and S. Kawata, *Journal of Raman Spectroscopy* **43**, 1177–1182 (2012).
- [85] B. Ren, G. Picardi, and B. Pettinger, *Review of Scientific Instruments* **75**, 837–841 (2004).

- [86] C. C. Neacsu et al., *Physical Review B* **73**, 193406 (2006).
- [87] N. Hayazawa et al., *Japanese Journal of Applied Physics* **46**, 7995 (2007).
- [88] T.-a. Yano et al., *Applied Physics Letters* **91**, 121101 (2007).
- [89] K. Uetsuki et al., *Nanoscale* **4**, 5931–5935 (2012).
- [90] A. Downes, D. Salter, and A. Elfick, *The Journal of Physical Chemistry B* **110**, 6692–6698 (2006).
- [91] C. Schäfer et al., *Nanoscale* **5**, 7861–7866 (2013).
- [92] S. Cherukulappurath et al., *Nano letters* **13**, 5635–5641 (2013).
- [93] J. Renger et al., *JOSA A* **21**, 1362–1367 (2004).
- [94] C. A. Barrios et al., *The Journal of Physical Chemistry C* **113**, 8158–8161 (2009).
- [95] N. Mauser and A. Hartschuh, *Chemical Society reviews* **43**, 1248–1262 (2014).
- [96] R Zhang et al., *Nature* **498**, 82–86 (2013).
- [97] H. K. Wickramasinghe et al., *ACS nano* **8**, 3421–3426 (2014).
- [98] J. Steidtner and B. Pettinger, *Review of Scientific Instruments* **78**, 103104 (2007).
- [99] B.-S. Yeo et al., *Applied spectroscopy* **60**, 1142–1147 (2006).
- [100] B.-S. Yeo et al., *Analytical and bioanalytical chemistry* **387**, 2655–2662 (2007).
- [101] M. Zhang et al., *Journal of Optics* **15**, 055006 (2013).
- [102] N. Kumar, A. Rae, and D. Roy, *Applied Physics Letters* **104**, 123106 (2014).
- [103] A. Taguchi et al., *Optics express* **17**, 6509–6518 (2009).
- [104] J. M. Klingsporn et al., *The Journal of Physical Chemistry Letters* **5**, 106–110 (2013).
- [105] C. Blum et al., *Journal of Raman Spectroscopy* **45**, 22–31 (2014).
- [106] M. B. Raschke and C. Lienau, *Applied Physics Letters* **83**, 5089–5091 (2003).
- [107] G. Picardi et al., *The European Physical Journal Applied Physics* **40**, 197–201 (2007).
- [108] A. Wiener et al., *Nano letters* **12**, 3308–3314 (2012).
- [109] R Ramos and M. Gordon, *Applied Physics Letters* **100**, 213111 (2012).
- [110] X. Cui et al., *Optics express* **15**, 8309–8316 (2007).
- [111] L. Novotny and N. Van Hulst, *Nature Photonics* **5**, 83–90 (2011).
- [112] C. C. Neacsu et al., *Nano letters* **10**, 592–596 (2010).
- [113] T. Umakoshi et al., *Applied Physics Express* **5**, 052001 (2012).
- [114] S. Kharintsev et al., *Journal of Physics D: Applied Physics* **46**, 145501 (2013).
- [115] I. Maouli et al., *Applied Physics Express* **8**, 032401 (2015).
- [116] Y. Zou et al., *Applied Physics Letters* **94**, 171107 (2009).
- [117] F. Huth et al., *Nano letters* **13**, 1065–1072 (2013).
- [118] A Weber-Bargioni et al., *Nanotechnology* **21**, 065306 (2010).
- [119] M. Fleischer et al., *ACS nano* **5**, 2570–2579 (2011).

- [120] P. Uebel et al., Applied Physics Letters **103**, 021101 (2013).
- [121] A. I. Denisyuk et al., Journal of nanoscience and nanotechnology **12**, 8651–8655 (2012).